



Optimization of the process-route of a Nickel-base alloy

Investigation of Sigma-phase precipitation in heat treatment

Optimering av tillverkningsväg för en Nickelbaslegering
Undersökning av Sigmafas-utskiljning i värmebehandling

Felix Andersson

Faculty of Health, Science & Technology

MSAE01 Degree project for Master of Science in Mechanical Engineering

30HP

Supervisor: Katerina Chantziara

Examiner: Mikael Grehk

2023-08-03

Abstract

The focus of this master's thesis is on the heat treatment of Ni-base alloys, specifically the risk of intermetallic σ -phases during different stages of heat treatment. The alloy studied is Sanicro[®] 28, a super-austenitic stainless steel produced by Alleima AB. The problem at hand is that the quench-annealing stage is in high demand at the manufacturing facility, and the goal is to investigate if it can be removed from the manufacturing route.

During forging, the outer surface and bar-ends can reach low temperatures, posing a high risk of σ -phase precipitation. Additionally, a necklace structure with large grains surrounded by fine re-crystallization is often observed at the surface of forged superalloys/Ni-base alloys. Today, this forged structure is re-crystallized and σ -phase dissolved during the quench-annealing stage. An alternative to quench-annealing after forging is to re-heat the bar using a Car Wagon Furnace (CWF).

The thesis includes two laboratory experiments simulating two stages of heat treatment, the CWF and induction furnaces/soaking.

The samples subjected to simulated CWF treatment showed re-crystallization throughout the entire structure. Annealing in CWF removes the large grains in surface positions. The time in the CWF also showed to be sufficient to dissolve σ -phase present from forging.

Samples heated to the induction furnace set temperature do not contain precipitates, while temperatures below the induction set temperature induce σ precipitation to varying degrees.

The key findings of the thesis are as follows:

- Re-heating in a CWF right after forging is enough to dissolve σ -phase at half-radius and surface locations.
- Quench-annealing stage could be removed by changing the route to a CWF after forging.
- If temperatures fall below the σ -maximum stability temperature during induction furnace heating cycles, σ -phase precipitation occurs.

Sammanfattning

Arbetet i denna rapport fokuserar kring värmebehandling hos Nickel-bas legeringar, specifikt risken av σ -fas utskiljning under olika värmebehandlings-steg. Legeringen som har studerats är Sanicro[®] 28, en av Alleima AB's superaustenitiska rostfria stål. Problemet som grundar detta arbete är värmebehandlingen släckglödning vid stegbalksugn 98 agerar flaskhals i fabriken. Målet är att tillämpa ett alternativ till släckglödning hos värmebehandlings-stegen hos Sanicro[®] 28.

Under smide så kan yttemperaturer och ändrar av en stång nå låga temperaturer, ner mot 850°C. Detta bidrar till en hög risk för σ -fas utskiljning vid dessa ytor. Ytstrukturen har, efter smide, en så kallad "halsbandsstruktur" med enorma korn blandat med små korn och σ -fas mellan dessa stora korngränser. Släckglödningssprocessen upplöser denna σ -fas och rekrytalliserar denna struktur. Ett alternativ till släckglödning, som djupgående har undersökts i detta projekt, är en återläggning i vagnugn (ÅVU) direkt efter smide.

Under vidgning och extrusionsprocessen, bidrar induktionsugnar svårigheter med att homogent värma upp kutsar inför respektive process. Att uppnå homogena temperaturer har visats vara utmanande och detta önskas kartläggas.

Projektet innehåller två områden av värmebehandlingsexperiment i laboratisk miljö, simulering av ÅVU samt undersökning av induktionsugnar och hållningsugn.

Proverna som undersöktes i ÅVU visade fullständig rekrytallisering av tidigare struktur, även komplett upplösning av σ -fas.

Prover som värmts till induktionsugnens process temperatur visade upplösning av σ -fas. Medans temperaturer lika med och under topptemperatur för σ -fas utskiljning visade större mängder av σ -fas.

Nyckel-slutsatser i denna rapport inkluderar:

- ÅVU i direkt efter smide kan upplösa all σ -fas som bildas under smide.
- Steget släckglödning kan, enligt gleeble experiment, ersättas utav ÅVU efter smide.
- Ifall temperaturer understiger topptemperatur för σ -fas utskiljning under induktionsvärmning förefaller σ -fas utskiljning

Acknowledgement

I would like to express my deepest gratitude towards Alleima AB and my supervisors Fredrik Sandberg & Anders Ulfvin for giving me the opportunity to do my master thesis at the company. Fredrik has shared invaluable expertise in heat treatment and materials science, helped me with experimental planning as well as support and mentorship throughout the project. Anders has shown exceptional insight into the expansion and extrusion processes and has also advised and supported me through the project.

Additionally, I would like to thank my supervisor Katerina Chantziara at Karlstad University for her dedication, support and guidance to help me finish a complete thesis. From her, I got supervision and insight into planning, writing and structuring the project.

I would also like to express my appreciation to additional individuals at Alleima AB who generously contributed their time and knowledge to this study:

- > Munir Al-Saadi, who helped me analyze samples in SEM and EDX, as well as sharing his expertise in materials science.
- > Fredrik Meurling, for taking his time and effort to discuss and share his experience into the project.
- > Anders Bergman, who sacrificed many hours into conducting my heat treatment experiments
- > Conny Sand, who dedicated many hours into preparing and polishing my samples

Lastly, I am grateful for my family and friends who have encouraged and supported me throughout my whole education.

For this, I am most grateful, thank you!

Sine Cera

Felix Andersson

August 3, 2023

Sandviken, Sweden

Contents

1 Introduction	1
1.1 Background	1
1.2 Problem description	1
1.3 Project purpose and objectives	1
2 Nickel-Base Alloys	2
2.1 Microstructure	3
2.1.1 Effect of Carbon content	4
2.1.2 Austenitic phase	5
2.1.3 Ferritic phase	6
2.1.4 Sigma Phase	7
2.1.5 Precipitates and carbides	8
2.2 Element segregation	9
2.3 Stress corrosion cracking	10
2.4 Sensitization	10
3 Sanicro[®] 28	11
3.1 Phases of Sanicro [®] 28	12
3.1.1 Grain size	13
3.1.2 Presence of Mo	13
3.2 Manufacturing stages	14
3.2.1 Casting	14
3.2.2 Diffusion annealing	14
3.2.3 Forging	14
3.2.4 Quenching	15
3.2.5 Quench-annealing	16
3.2.6 Car Wagon Furnace reheating	16
3.2.7 Expansion and extrusion stages	17
3.2.8 Billet induction heating before expansion (Heating 1)	18
3.2.9 Expansion	19
3.2.10 Billet induction heating before extrusion (Heating 2)	19
3.2.11 Extrusion	19
3.3 Previous work on Sigma precipitation in Sanicro [®] 28	21
3.3.1 Development of a dissolution-diagram for sigma in a Sanicro [®] 28 rod	21
3.3.2 Documentation of microstructure of an ingot cast San28Cu bar	22
3.3.3 TTP-diagram for Sanicro [®] 28	23
3.3.4 Precipitation Kinetics of Sigma Phase during Extrusion of San28Cu tubes	23

4 Method	24
4.1 Material	24
4.1.1 Quench-annealed samples	24
4.1.2 Forged samples	25
4.2 Experimental procedure	26
4.2.1 Gleeble Heating 1 induction furnace experiments	27
4.2.2 Gleeble Heating 1 stop scenario experiment	28
4.2.3 Gleeble soaking experiment	29
4.3 Re-heating in CWF after forging experiments	29
4.3.1 Computed simulation of reheating in CWF	29
4.4 Gleeble Reheating CWF experiment	29
4.5 Sample preparation	30
4.6 LOM	30
4.7 SEM/EDX	30
5 Results	31
5.1 Simulation of Re-heating in a Car-wagon furnace	31
5.2 Analysis of Gleeble CWF experiment	32
5.3 Analysis of Expansion/Extrusion experiments	35
5.3.1 SEM & EDS analysis for Heating 1 experiments	38
5.3.2 Analysis of Heating 1 stop scenario	40
5.3.3 Analysis of soaking experiments	41
6 Discussion	43
6.1 Samples	43
6.2 Deformation	43
6.3 QAsc3 result variation	44
6.4 CWF implementation	45
6.5 Induction heating and soaking implementation	45
6.6 Full-scale experiments	46
7 Conclusions	47
7.1 Future Work	47
References	48

Abbreviations

Ni	Nickel
SCC	Stress Corrosion Cracking
σ	Sigma
γ	Gamma
δ	Delta
Wt%	Weight Percentage
Cr	Chromium
α	Alpha
C	Carbon
N	Nitrogen
FCC	Face-Centered-Cubic
BCC	Body-Centered-Cubic
Fe	Iron
Mo	Molybdenum
Si	Silicon
$T_{\sigma MST}$	Sigma Maximum Stability Temperature
DRX	Dynamic Re-crystallization
WBF	Walking Beam Furnace
IRF	Industrial Reheating Furnace
CWF	Car-Wagon Furnace
TTP	Time Temperature Precipitation
LOM	Light Optical Microscopy
SEM	Scanning Electron Microscopy
EDX	Energy Dispersive X-ray spectroscopy
Al	Aluminium
Mg	Magnesium

1 Introduction

1.1 Background

High percentage Nickel (Ni) austenitic alloys were developed to prevent Stress Corrosion Cracking (SCC) in extreme corrosive and high temperature environments. This was achieved by alloying with a high percentage of Ni, thus they became more commonly known as Ni-base alloys or Ni-base stainless steels. Their exceptional corrosive resistance and mechanical strength allow these alloys to be used in very diverse conditions.

Sanicro[®] 28 is a Ni-base alloy commonly used in high demanding applications like strong acid piping and nuclear power plants. The alloy is produced by Alleima AB, a world-leading company of advanced steel and other high-end alloys.

The line of manufacturing and individual stages of heat treatment for Sanicro[®] 28 is currently casting, diffusion annealing, forging, quench-annealing and heating before expansion and extrusion. This is a relatively long and complicated production chain where the properties of the alloy are determined at every stage of deformation and heat treatment.

1.2 Problem description

During heat treatment of Ni-base alloys, there is a risk of intermetallic Sigma (σ)-phases to grow. This is a highly undesired phase since it reduces the impact toughness, and the fatigue life at elevated temperatures.

The quench-annealing stage at Alleima AB is at high demand at the facility. Many products and materials are heat treated at this stage, causing it to very often be occupied. Due to this fact, the ideal scenario for the facility would be to remove quench-annealing from the manufacturing of Sanicro[®] 28 without interfering with the final properties of the product.

The goal of the present effort is to study σ -phase precipitation at the individual stages of heat treatment. Thus it will be possible to determine if Sanicro[®] 28 could be manufactured without quench-annealing or not.

1.3 Project purpose and objectives

The purpose of this thesis is to make the production of Sanicro[®] 28 more efficient. This means that one of the stages of heat treatment ought to be removed due to its high demand in production. To achieve this, research and knowledge of σ precipitation at several heat treatment processes need to be acquired. As well as gathering and summarizing previous work done on the matter.

2 Nickel-Base Alloys

The development of Ni-base alloys began when the properties of austenitic stainless steel did not match the environmental challenges of high temperature creep strength and SCC.

In many categories austenitic stainless steel and Ni-base alloys are similar, however, the increased content of Ni acts beneficial to the prevention of SCC. All together, many of the properties, phases, microstructure and heat treatment theories can be equalled to those of austenitic stainless steels with over 20% Ni [1].

Stainless steels, austenitic stainless steels and Ni-base alloys consist of primarily two important phases which correspond with gamma (γ) - austenite and delta (δ)- ferrite. The amount of each respective phase changes the properties and the primary phase of the alloy. When alloying with a high weight percentage (wt%) of Ni and Chromium (Cr) the primary phase obtains an austenitic and ferritic structure respectively. This relationship can be observed in Fig 1. The material analyzed in this thesis Sanicro[®] 28 has the Ni_{eq} and Cr_{eq} 32.5% and 33.4% respectively, calculated from eq 1 and 2. A martensitic phase can also be obtained for some Ni-base alloys when the carbon content is high and Ni or Cr wt% is low if the material is also heat treated correctly. In alloys rich in austenite, some Martensite can form for example when cold rolling, in case the transformation temperature for martensite M_s is high enough. [2, 3].

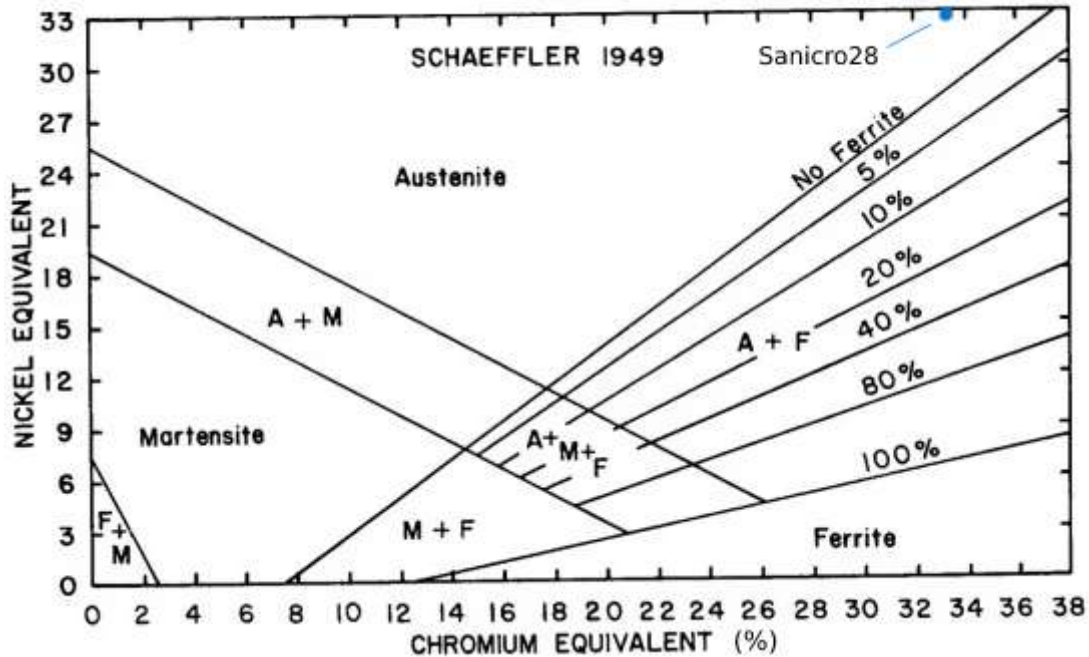


Figure 1: Schaeffler diagram [4], the blue dot indicates Sanicro[®] 28

Ni-base alloys exhibit excellent corrosion resistance against strong acid environments like chlorides and sulphur, together with high mechanical strength, work at elevated temperatures, formability and weldability the alloys are very functional at piping, tubes and heat exchangers [5].

The properties of Ni-base alloys can be altered via other alloying elements depending on what

properties that are desired for the various environments. Some elements will stabilize the γ -phase, and some the δ -phase which are referred to as the Ni- and Cr equivalents, which can be seen in Eq 1 & 2. The equations are commonly used in the Schaeffler diagram to specify stainless steels, as seen in Fig 1, even though this is not a phase equilibrium diagram.

$$Ni_{eq} = Ni + Co + 0.5Mn + 30C + 0.3Cu + 25N \quad (1)$$

$$Cr_{eq} = Cr + 2.0Si + 1.5Mo + 5V + 5.5Al + 1.75Nb + 1.5Ti + 0.75W_{wt\%} \quad (2)$$

The equivalent content of Ni and Cr is commonly used to name different types of Stainless Steels because they strongly correlate with the properties of the material. The Ni_{eq} components like Mn, C and N are used to improve solubility, precipitation strengthening and creep life respectively [6].

2.1 Microstructure

The microstructure of Ni-base alloys consists primarily of the γ -phase as the main phase with small amounts of α/δ -phase growing between the γ grain boundaries. When an excess of Ni_{eq} or Cr_{eq} exists, or alloying with a lot of other elements, then precipitates, carbides and intermetallic phases grow. Some or many of those phases are either problematic or intended for improving material's properties. The formation of the phases is mainly controlled by heat treatment since some precipitates grow at certain temperature intervals.

The phase equilibrium of Sanicro[®] 28 Ni-base alloy can be described using the Ni-Cr binary phase diagram, Fig 2. The austenitic phase is the dominant phase and will nucleate from 1400°C down to 600°C. To obtain the austenitic structure, heat treatment is commonly made at these temperatures and then quenched to retain the austenitic structure. To further explain the characteristics of Sanicro[®] 28, a more detailed phase diagram is needed to observe all possible phases, (section 3.1).

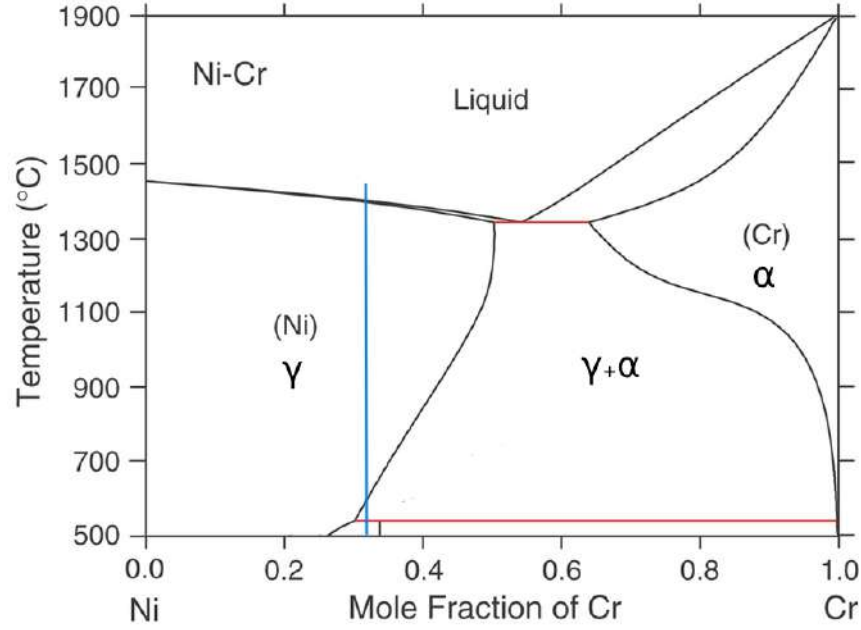


Figure 2: *Ni-Cr binary phase diagram [7], blue line indicates the temperature phase transitions of Sanicro[®] 28*

2.1.1 Effect of Carbon content

Carbon (C) in austenitic stainless steel is problematic and can affect both strength and the corrosive behaviour. C can strengthen austenitic stainless steel by occupying interstitial sites within the crystal lattice. This leads to distortion in the matrix and increases the strength of the material. However, a too high amount of C can effectively cause the material to instead become brittle because of high amounts of carbide formation. When there is high amounts of Cr and C they can form $M_{23}C_6$ and M_7C_3 carbides. These carbides are the main reason for intergranular corrosion/sensitization to occur [8] (Further explained in section 2.4). The formation of $M_{23}C_6$ and M_7C_3 can be seen in Fig 3.

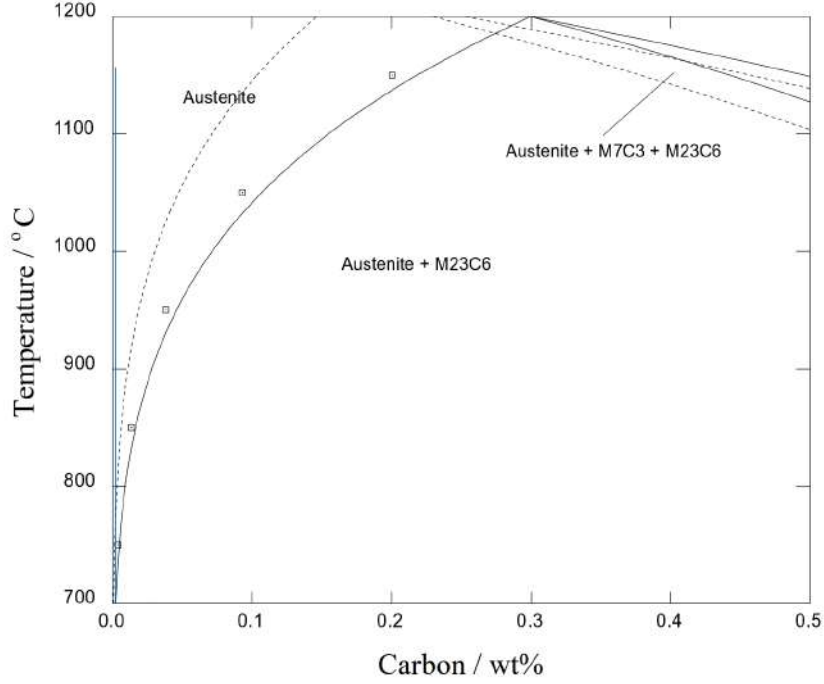


Figure 3: The formation of $M_{23}C_6$ and M_7C_3 [6], the thin blue line indicates Sanicro[®] 28 at nominal 0.02% C (0.0002 wt% in diagram)

From the decrease of C content and a simultaneous increase of the heat treatment temperature, the formation of $M_{23}C_6$ and M_7C_3 is decreased. To prevent intergranular corrosion/sensitization, therefore many Ni-base alloys have very low levels of carbon, $<0.08\%C$ [1]. It is also possible to avoid the precipitation of M carbides (M referring to carbide formers) by replacing C with Nitrogen (N). N is often the suitable alloying element instead of C as the atomic size is similar and thus has similar solid solution strengthening mechanism. It stabilizes austenite and do not react into Cr and Ni to form M carbides. However, N can consume Cr and instead form Cr-rich nitrides. [6]. Carbon can to some extent increase the yield strength of an austenitic stainless steel, however in higher concentrations, it can become brittle as well as substantially decrease the supposed corrosion-resistant material. [9]

2.1.2 Austenitic phase

Austenite is Face-Centered-Cubic (FCC) and tends to be ductile in Ni-base alloys without solid solution strengthening. The possible austenite phase solidification is controlled by the amount of Ni, Cr, as well as C in the alloying composition, as can be seen in Fig 4 & 3. Ni expands the area of γ -phase growth, called the “ γ -loop” shown in the Fe-Cr diagram in Fig 5. If large enough, like in Nickel base alloys, the austenite will be able to retain during cooling, down to room temperature. Fig 4 shows the large area of austenite received when alloying with a high wt% of Ni. [8]

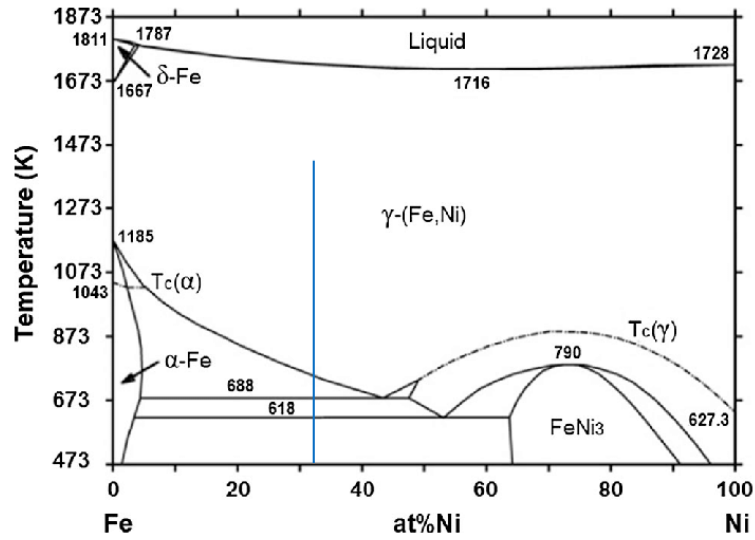


Figure 4: Binary Fe-Ni diagram [10]

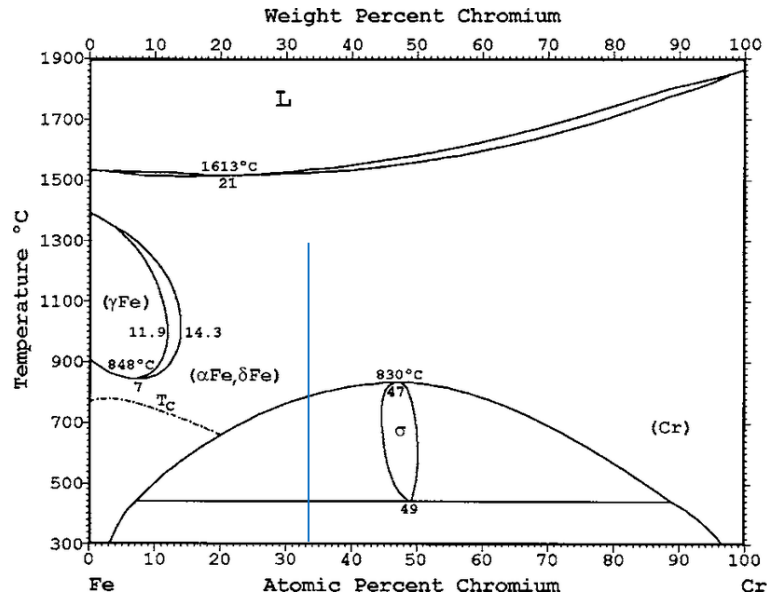


Figure 5: Fe-Cr binary system [11]

2.1.3 Ferritic phase

The δ ferritic phase is Body-Centered-Cubic (BCC) and stable over a wide range when the amount of Ni is lower than 8%. Ferrite contributes with great resistance to SCC in high temperature environments where the load is minimal. The reason ferritic stainless steel is not used in the same environments as Ni-base alloys is because of their difficulty to withstand creep at higher loads. In cases of a high wt% of Ni, the δ -phase is reduced. Instead, the δ -phase will grow between grain boundaries of the γ -phase. In the boundaries, there is now a lot of Cr and because Cr diffuses easily into other elements [6], many precipitates, as well as the intermetallic σ -phase grow at those areas. α is also a ferritic phase in stainless steels though it's not present as the main phase in cases where the wt% of Cr is higher than 12%. α may grow during tempering at lower

temperatures (see Fig 4 and it is known that some σ phases precipitate at these temperatures. [8, 2]

2.1.4 Sigma Phase

The intermetallic σ -phase precipitates from δ - ferrite in high Cr regions when the Cr wt% is over 20%. It consists of iron (Fe) and Cr around 30-50%. σ is stabilised by the amount of Cr in the alloy. Additionally, the stability can be increased by the presence of Molybdenum (Mo) and Silicon (Si). This will affect the range of σ equilibrium temperatures and the peak fraction. Mo tends to segregate into inner parts of a melted bloom or ingot when solidified, thus σ precipitation may be more evident in the segregated areas (further discussed in section 2.2 & 3.1.2).

Growth occurs commonly between 600°C to 1000°C. The region at which σ is present can be altered with Cr and Ni. At a binary Fe-Cr system, Fig 5, the σ -phase exists only up to 800°C. In Fig 6 are possible peaks of σ observed, here the temperature at which σ precipitation is fastest around 850°C [12].

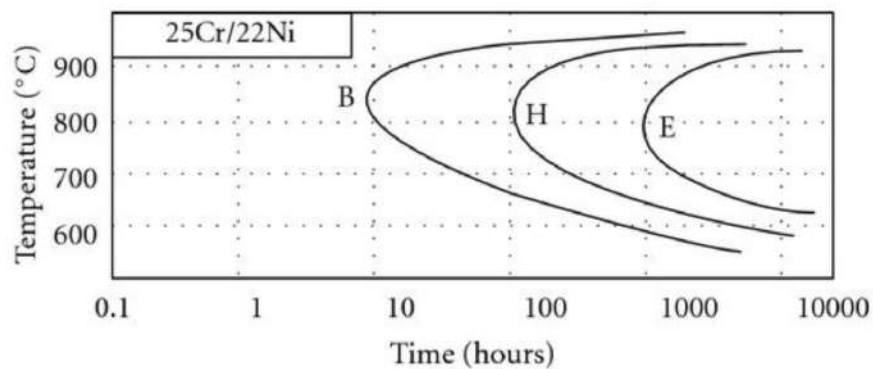


Figure 6: *TTT curve for σ precipitation in high Cr Ni (not Sanicro[®] 28) content (B: initial precipitation, H: Intermediate stage, E: final precipitation stage) [12]*

For higher Cr and Ni alloys, the σ -phase will precipitate up to 1100°C and will diffuse slower. Although diffusion is slower and has little presence, the presence of σ is highly undesired as it decreases the toughness and causes the alloy to be brittle. Brittleness is caused mostly by the tetragonal shape of the σ precipitates and if these are "joined" together in continuous lines between grain boundaries, it increases brittleness significantly. σ is also a hard precipitate with sharp edges, thus it is likely to initiate crack propagation which could cause the fatal failure. The structure of a σ precipitate has a large lattice mismatch with both ferrite and austenite. Therefore, the nucleation of σ is difficult and preferred precipitation occurs at high energy interfaces, like the grain boundary between γ grains as can be seen in Fig 7 [12, 6]

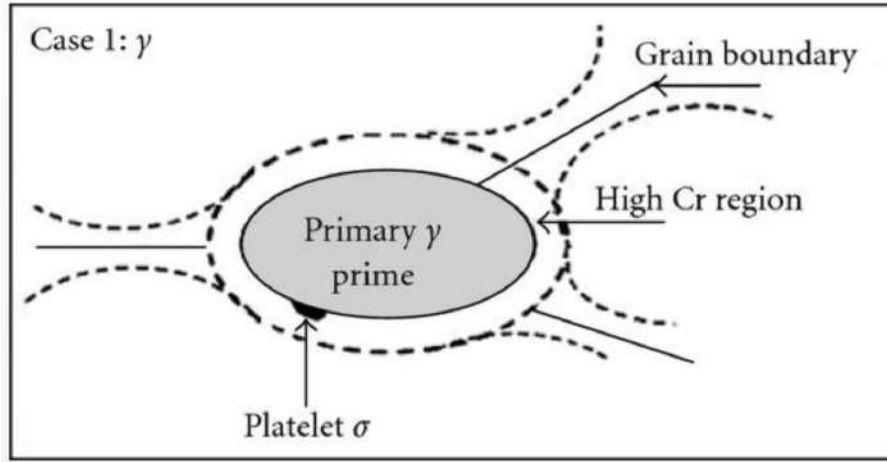
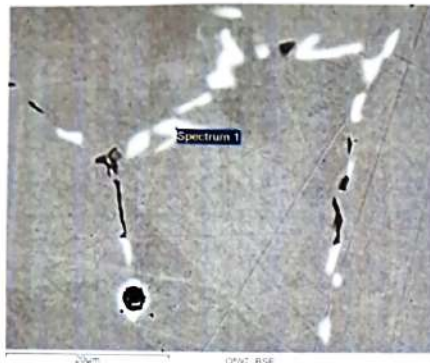


Figure 7: Common σ -phase precipitation in austenite [12]

The typical chemical composition of σ -phase is higher volume fractions of Cr and Mo, with a decrement in the amount of Fe and Ni. An example of the composition of a σ particle can be seen in Fig 8. Additionally, if rest particles of σ are present at extrusion the result will look different compared to Fig 8. In cases of large deformation like in extrusion, the particles will deform to lines/strokes.



Spectrum 1		
Element	Weight%	Atomic%
Si K	0.57	1.16
Cr K	40.65	44.63
Mn K	1.38	1.43
Fe K	29.56	30.21
Ni K	15.91	15.47
Mo L	11.93	7.10
Totals	100.00	

Spectrum processing :
 No peaks omitted
 Processing option : All elements analyzed (Normalised)
 Number of iterations = 3

Figure 8: Common σ -phase composition seen in a particle

It is possible to dissolve the σ -phase through re-crystallisation or dissolution if temperature and holding time are high enough. Re-crystallisation occurs at a few stages of the heat treatment process of Sanicro[®] 28 and can dictate the volume fraction of σ in the final product. There are some limitations when σ has been present and then dissolved. In this stage, just after dissolution, some alloying elements are still left at the location with a composition similar to that of σ . Re-precipitation of σ is more likely because the composition is already present and therefore it precipitates with less resistance.

2.1.5 Precipitates and carbides

MX – Carbides

MX are strong carbide and nitride formers, M represents carbide or nitride formers and X represents C or N. When a fine dispersion of MC carbides are present in Ni-base alloys they contribute

to strength and in particular during creep deformation. Some variations of MX carbides are undesired because they can decrease for example corrosion performance.

$M_{23}C_6$

The carbide nucleates easily at early stages of precipitation at all temperatures. It diffuses with Cr and grows in grain boundaries because the lattice is about three times larger than that of the austenite [6]. In Sanicro[®] 28 $M_{23}C_6$ has little presence because of the low amount of C in the alloy.

M_6C

The M_6C is an FCC carbide which forms with varying compositions but is most evident in Mo- or Nb-rich alloys. In contrast to $M_{23}C_6$, M_6C is rich in Ni instead of Cr.

Gamma – Prime

γ' precipitates exhibit a similar structure to that of the γ -phase and are formed during ageing with Nickel, titanium and aluminium at around 600°C. The phase can be observed at the lower temperature stage on the line in Fig 2. These precipitates give the Ni-base alloys some of their strength. However, it is not recommended to strengthen with γ -phase because at 600°C, the brittle σ -phase will also form and weaken the material. [13]

Chromium – nitrides

Chromium Nitrides (Cr_2N or M_2N) is a type of compound in which N together with Cr forms hexagonal precipitates. It is most common in duplex stainless steels but can be present in austenitic if N levels are sufficient. [14]

Laves – phase

Laves phase is an intermetallic phase that forms equiaxed particles with hexagonal shape on grain boundaries. It has some effect on creep and the formation of M_6 . Because Mo is present in Sanicro[®] 28, 3.0%, the growth of Laves can occur after long ageing times. Though its formation is limited by δ -ferrite in grain boundaries [6].

2.2 Element segregation

The temperature to volume fraction observed in Fig 9 is at a nominal composition of alloying elements. Products that reach the nominal composition have elements evenly distributed throughout the metal. This is difficult to achieve in a processed product and could cause defects to the final product if variations are too high. The variations often originate from the melting and casting stage. Atomic weights, density, bonds, entropy etc, can cause variations in elements in the cast ingot. Mo is one of the elements that are prone to segregate, that especially have been seen to vary in Sanicro[®] 28 and to segregate towards the inner volume of the ingot.

The segregation of Mo is at both macro- and micro-scales. The micro-segregation occurs between dendrites and is often possible to even out during diffusion-annealing. The more problematic segregation is at the macro-scale because this can impact the properties and the precipitation

kinetics. Here, Concentrations are seen to radially differ radially into layers towards the central axis and is often at most at the centre. The variation will locally change the composition of the alloy and the equilibrium temperatures will therefore differ in comparison to Fig [9](#) [\[2\]](#)

2.3 Stress corrosion cracking

SCC is an environmentally assisted cracking induced mechanism caused commonly when metal or an alloy is exposed to acid under sustained loads (as low as 5% of the yield stress). It's a form of sub-critical cracking that propagate from microscopic cracks under the influence of loads and chemicals. General corrosion and deformation is not seen while a surface is attacked from SCC and the surface could meanwhile be bright and shiny. Therefore, SCC is very difficult to detect, and because of its microscopic scale, it could cause failures without prior warning. [\[15\]](#)

2.4 Sensitization

Sensitization is a type of intergranular corrosion and is an effect of local matrix depletion of Cr surrounding high Cr precipitates. Carbides and precipitates in high Cr stainless steels and alloys contain high levels of Cr in their composition. an example of high Cr can be seen in the σ -phase in Fig [8](#). When Cr-rich precipitates, like σ -phase, are present in grain boundaries they "consume" the surrounding Cr from the local matrix. This is where intergranular corrosion is prone to occur because the lack of Cr causes a reduction in passivation. This mechanism is called the Cr depletion theory and is the most common and accepted theory. [\[16\]](#)

3 Sanicro[®] 28

The alloy studied in the present thesis is Sanicro[®] 28 which is one of Alleima AB's high-performance super-austenitic stainless steels. The alloy is standardized according to UNS: N08028, ISO: 4563-080-28-I & DIN: X 1 NiCrMoCuN 31 27 4. It's specifically designed for pipes and tubes in strong acid environments because it exhibits good resistance to general, intergranular, pitting and crevice corrosion, SCC and also has great weldability when joining pipes.

The high amount of Cr in Ni-base alloys accounts for almost all corrosion resistance properties, like in austenitic and stainless steels. The Cr forms a thin layer of regenerative passive film that protects the alloy from corrosion. Sanicro[®] 28 was originally designed to endure phosphoric acid environments where corrosive chlorides are present. These chlorides induce SCC, especially if the temperature is high. With a high wt% of Ni in Sanicro[®] 28, SCC is very limited.

The chemical composition is primarily Ni, Cr and Fe, Ni and Cr having a higher wt% than Fe combined. The nominal composition can be seen in table [1](#). The rest is pure iron.

C	Si	Mn	P	S	Cr	Ni	Mo	Cu	N
≤0.020	≤0.7	≤2.0	≤0.020	≤0.010	27	31	3.32	1.0	≤0.1

Table 1: *Chemical composition of Sanicro[®] 28 (nominal) %* [\[5\]](#)

The alloy and its mechanical properties are designed for high temperature environments, although its use is limited to under precipitation temperatures at 600°C. At >600°C for prolonged periods, precipitation causes embrittlement and could damage the alloy. Beneath and down to cryogenic temperatures, the alloy exhibits high impact strength because of its austenitic structure [\[2\]](#). The alloy exhibits high strength from room temperature to 550°C, especially cold worked tubes that are suited for oil and gas production. [\[5\]](#).

3.1 Phases of Sanicro[®] 28

The microstructure and phases are controlled during the manufacturing of Sanicro[®] 28 at the different stages of heat treatment and will differ depending on temperatures and rate of deformation. At certain stages the outer surface may look different to the inner parts of a heated bar because of material temperature gradients. If the temperatures differ there may be parts of the bar that are in the temperatures of σ -phase precipitation. This could for example happen at forging when the outer surface will cool at a higher rate than the inner volume. The outer surface and bar-ends can experience lower temperatures at certain stages and could be at high risk of σ precipitation. The individual stages of heat treatment and possible σ presence will be explained in section 3.2. Although there's a large mixture of phases and precipitates, Sanicro[®] 28 and other Nickel-base alloys are commonly not processed at temperatures lower than 1100°C. Instead, the alloy is quenched at higher temperatures to retain the fully austenitic structure that will form above 1100°C.

From the chemical composition in table 1 and the phase diagram in fig 9, the following phases, intermetallic phases and precipitates can be present in a nominal composition. Over 1100°C only austenite grows and often form twin boundaries. At around 400-600°C, Cr will start to diffuse into the FCC austenitic matrix and form BCC δ . The low amount of C prevents $M_{23}C_6$ and M_6C to precipitate. Mo and Si together with Cr account for σ precipitation in Sanicro[®] 28, from 600-1100°C, with a maximum fraction at 700°C. Mo is also the reason that Laves phase can be present and grows at around 700°C down to room temperature.

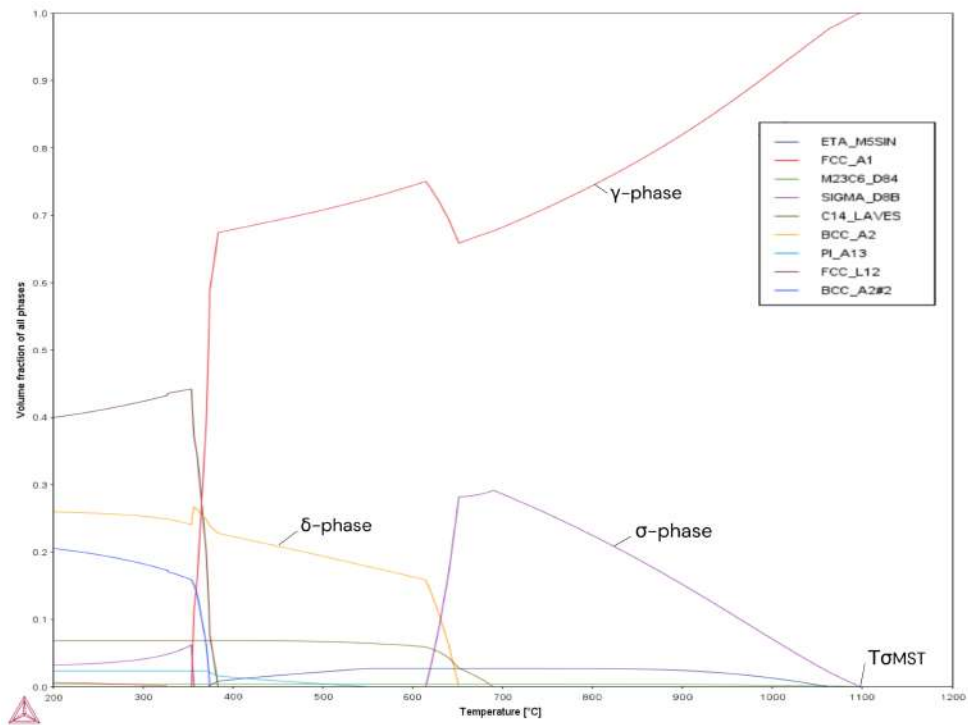


Figure 9: Sanicro[®] 28 phase-equilibrium diagram calculated using Thermocalc, σ is shown as purple from 600-1100°C, with a maximum fraction at 700°C, $T_{\sigma MST}$ here is 1100°C

3.1.1 Grain size

Grain sizes are measured and determined through ASTM E112-13(2021) [17]. The most common is the intercept method where lines are overlayed on an image of grains which then are dotted to indicate grain boundary positions. Grain size is then calculated using the distances between dots on the overlayed lines. [18]

The scale of number G (ASTM grain size number) starts at 00 and as this number increases the actual average area of a grain measured is decreasing. This is to say that $G = 00$ is the largest available measurement of grains using ASTM E112-13.

In production at Alleima AB, tubes are quality controlled with ultrasonic testing to ensure that no flaws like cracks are present in the product. There are however limitations with ultrasonic testing. A product of grain size $G \leq 1$ will be too large to be measured and the product will be dismissed. Apart from mechanical properties obtained from grain size, $G > 1$ is the accepted ASTM grain size before ultrasonic testing.

It is commonly known that decreasing grain size increases strength of a metal alloy. [2] As such, the product properties are much dependent on grain size control and keeping grain sizes small. This is achieved by re-crystallization at stages where the temperature is high enough to induce nucleation of new grains.

3.1.2 Presence of Mo

Increased wt% of Mo is known to raise the peak volume fraction of σ , as well as the temperatures where σ -phase will precipitate [12]. It can be illustrated through a varied nominal composition calculated in Thermocalc and values illustrated through Excel. Shown in Fig 10 is an example of variation in σ Maximum Stability Temperature ($T_{\sigma MST}$), which is nominally 1100°C in Fig 9, when Mo is varied around the nominal composition, from 2.5-4.5wt%. In practice, Kolmskog [19] experimented and showed that an increment of 0.4wt% at a local area ($x \times x \mu m$) of Mo could raise $T_{\sigma MST}$ with 30°C in Sanicro[®] 28. The composition of a common σ -particle was illustrated earlier, Fig 8. This is a much higher wt% compared to Fig 10. This is not accurate if the dissolution temperature is sought and is only to illustrate the composition and detection of the precipitate. It's important that the measurement is done over a generalized area.

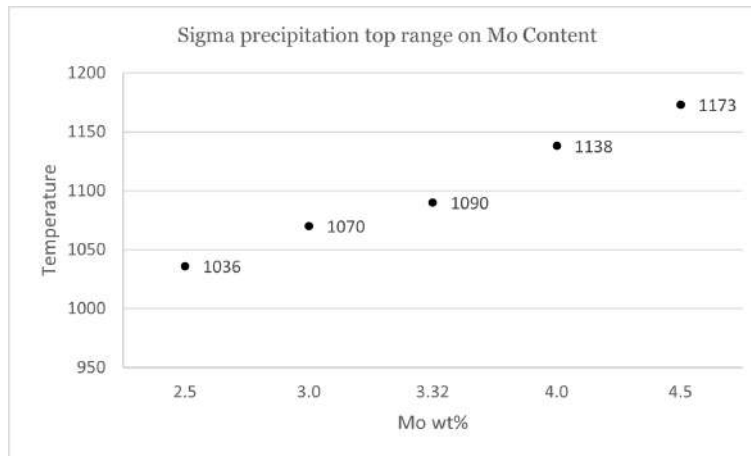


Figure 10: Mo wt% affecting $T_{\sigma MST}$, temperatures calculated using Thermocalc

3.2 Manufacturing stages

The diagram in fig 9 shows the theoretical phases growing at certain temperatures at equilibrium. Further in this section, σ precipitation at each stage of the relevant manufacturing and heat treatment processes will be explained with theory and observations made internally at Alleima AB.

3.2.1 Casting

At the melting and casting process the chemical composition is proceeded and can be traceable until the product is finished. The melt temperature is very high and is later water-cooled in first stage of continuous casting or cooled via the mould when poured into ingots. Sanicro[®] 28 is commonly cast into 27" ingots which will weigh up to 5.2 tonnes. The microstructure and forming are rarely set at this stage and are instead later improved at later heat treatment stages. Although some variation in chemical compositions in the form of segregation can impact the microstructure at later stages. The melting temperature can differ from segregated elements both at macro and micro-scale. Nylöf et al. [20, 19] mentioned in their studies that Mo can increase the stability temperature and peak of σ equilibrium and could cause local areas of increased precipitation. Although this is not a crucial difference and can be dismissed because the centre of the Sanicro[®] 28 bar is later removed at drilling in preparation for extrusion.

3.2.2 Diffusion annealing

After the bar has been pre-rolled in a blooming mill to the desired dimension it's heat-treated by diffusion annealing. Properties and microstructure are enhanced by long exposure of high temperatures. The main purpose of this is to even out segregation of elements [2]. At the end of the diffusion, the alloy will be closer to the nominal composition and grain sizes will be very large. For Sanicro[®] 28, the annealing time is usually many hours. From experimental data [20], all σ precipitation is dissolved if referring to Fig 9, 18 & 19.

3.2.3 Forging

Before the forging process the material is re-heated to above σ equilibrium, forged and then quenched in water. Forging takes place in a time span that allows the outer surface to cool down to critical temperatures where there's risk of σ precipitation. According to Vander Voort [21], a necklace structure, a type of dynamic re-crystallization (DRX), is often found in superalloys/Ni-base alloys when it's been forged. Large grains are surrounded by fine re-crystallization in those large grain boundaries. The deformation that takes place will cause a large stress-strain mismatch and will cause nucleation of new fine grains between the old. Progressing strain during the forging causes high density of dislocations at the new re-crystallized grains, which in turn reduces further grain growth beyond the large grain boundaries. [22]

The inner volumes of a forged bar won't deform as much as the outer volume and will also retain high enough temperatures to re-crystallize the structure into fine grains. The outer surface during forging allows DRX at the deformed volumes and because temperatures are lower, σ is prone to precipitate here.

Nylöf et al. [20] conducted an experiment that showed that the structure of a Sanicro[®] 28 rod at forging shows DRX at the outer surface and σ between fine grain boundaries. At the outer surface, 20 mm deep, very large grains surrounded by bands of incipient re-crystallisation were shown. Large amounts of σ had precipitated within these bands, presented in Fig 11 structure A. At the duration of the forging, the outer surface is exposed to air cooling down to around critical σ peak equilibrium. The fraction of σ that precipitated at the outer surface is more problematic to dissolve when the rod is heated again at quench-annealing and expansion/extrusion because these are nucleated at high dislocation density sites, i.e high energy sites.

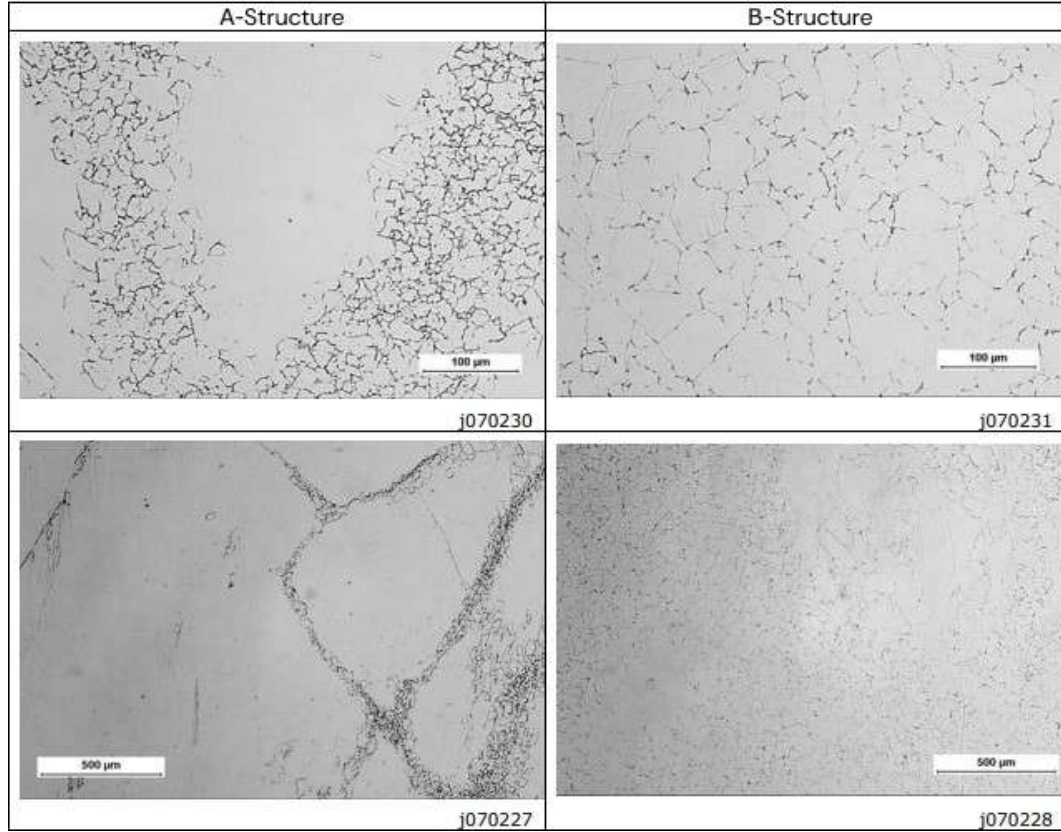


Figure 11: Structure after forging, structure A outer surface <20mm, structure B >45mm deep [20]

3.2.4 Quenching

Quenching is a procedure that is used to rapidly cool a material in order to "freeze" the microstructure in which there is little time for nucleation or growth/dissolution of grains. During quenching, the cooling rates at different positions of a bar or billet will be different. A larger billet will be slower to cool because the insides are only cooled via conduction from the outer surface in contact with the cooling liquid. This can be slow down to 30°C/min at half radius as seen in Fig 12 whereas the surface is almost instantly cooled. Compared to a bar, hollow bars are however more uniform to cool down due to the hollow centre.

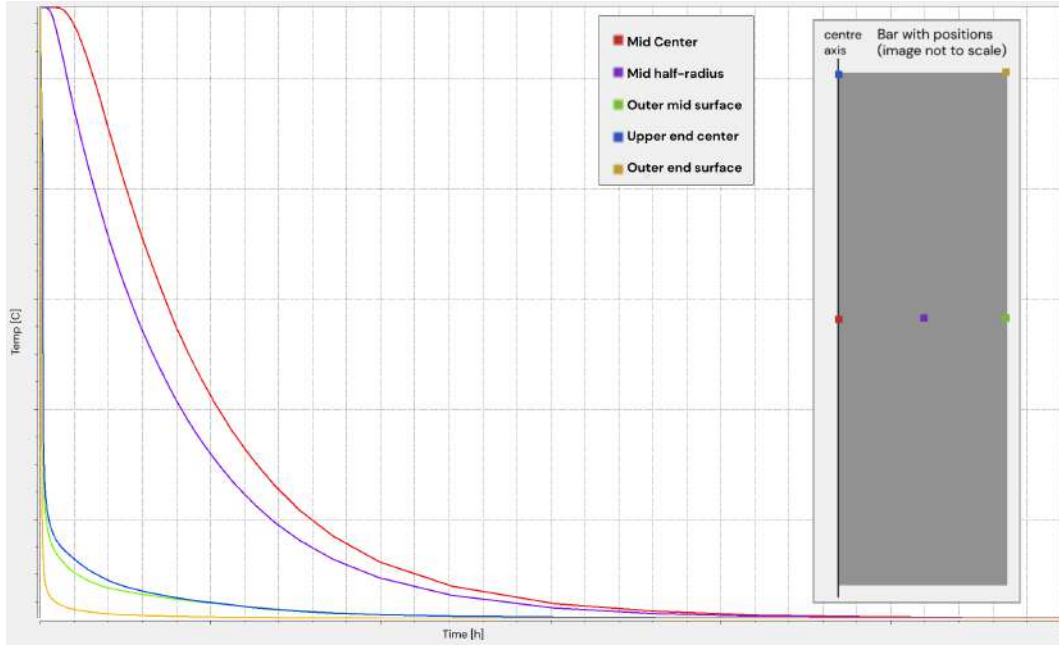


Figure 12: *Simulated cooling rate of quenching in water of a bar of Ø334mm*

3.2.5 Quench-annealing

Annealing is a process where dislocation density is reduced when the material is heated at medium-high temperatures at long holding times. It is a heat treatment stage used to dissolve or deny growth of precipitates. The high temperatures and long holding times will also re-crystallize the structure and allow grains to grow to large. The material is heated from room temperature up to the desired annealing temperature in a walking beam furnace (WBF), which is an Industrial Reheating Furnace (IRF). When the material has been held for a set time, which is very long, it's quenched by a cold stream of water and lastly cooled in air. The process stage was introduced as a solution to obtain a σ -free structure before expansion and extrusion.

3.2.6 Car Wagon Furnace reheating

Instead of quench-annealing a bar after forging an alternative process is to re-heat the bar right after forging, a type of annealing that is similar to quench annealing. The high temperatures will dissolve precipitates and unify the microstructure into fine re-crystallized grains across the volume. It can be accomplished with a Car Wagon Furnace (CWF) that is set to around the same temperatures as the diffusion annealing.

Reheating stage process is meant to save time by not having to heat the bar from room temperature if, as in the Sanicro[®] 28 process, quench-annealing is the next process step.

Temperatures during reheating would be sufficient to re-crystallize the outer surface necklace structure into a fine grain size instead of quenching at lower temperatures. The inner volume of the bar would not be drastically exposed to changes in temperature due to quicker heating from convection at the surface. As for the change in microstructure or increase in grain size for the inner volume, this has to be further investigated.

This stage is currently not in the manufacturing process of Sanicro[®] 28 but could be a potential

process route to investigate. Some products at Alleima AB are using this route as of today. In order to acquire the desired/respective microstructure, the annealing time in the CWF has to be studied as well as cooling temperatures at this stage.

A change to this stage could save energy consumption by reducing time in furnaces. Reheating in a CWF after forging would replace the WBF. Industrial Reheating Furnaces (IRF) is a large energy consumer for steel production. The time in the oven for Sanicro[®] 28 in quench annealing at the WBF is long. A change to the CWF could decrease the time in the furnace to below an hour. If this process route is possible it would decrease energy consumption by a substantial margin.

3.2.7 Expansion and extrusion stages

To illustrate the complete process of induction heating, expansion and extrusion, Fig 13 & 14 is presented below.

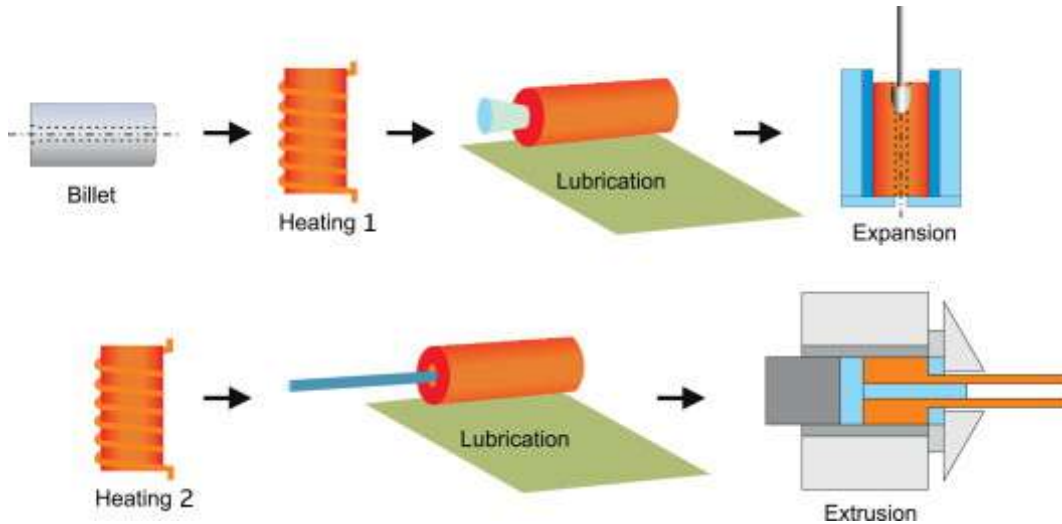


Figure 13: *Illustration of the expansion/extrusion stages* [23]

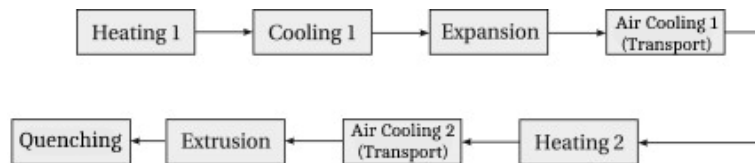


Figure 14: *Labelling for the expansion/extrusion stages* [23]

3.2.8 Billet induction heating before expansion (Heating 1)

The billets heated before expansion are heated in an induction heating furnace (Heating 1 in Fig 14). The physics behind induction heating differs from gas or electrical heating furnaces which induce heat by conduction and convection. At induction, heat is generated through an electric current that is produced when an electromagnetic field acts on the metal that is to be heated. Heating a metal is limited by how thick the workpiece is, the effective depth of heating depends on the frequency at which the current is generated and material properties like electrical resistivity and magnetic permeability [24]. In other words, it can be difficult to heat a thick wall billet because the depth of heating is limited to the outer surface. The inner surface will then only be heated through heat transfer by conduction and not induction.

The solution in these scenarios is to cycle the power when the outer surface reaches the desired temperature. When the power is off, the outer surface will cool while the inner surface will increase in temperature by conduction heat transfer from the outer surface. Therefore at the end of heating, the billet will be reaching more uniform temperatures.

Cycling is the solution for Sanicro28 billets because it's a large-dimension product. The thickness might therefore be larger than the depth at which heating is possible through induction. Usually, one cycle is used to get uniform temperatures.

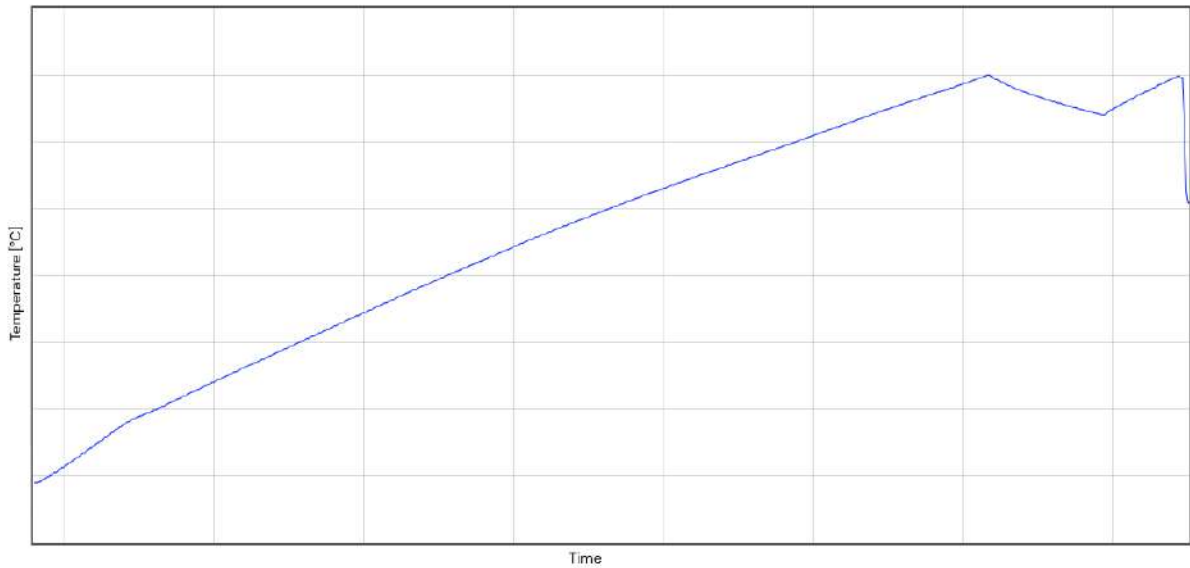


Figure 15: *Common temperature curve at outer mid surface for a billet heated and cycled in Heating 1*

In the production of Sanicro[®] 28 using induction heating, the temperature is set to above σ equilibrium and will be heated until it's reached and cycled 1 time. The inner surface will reach top temperature for a short period of time because of delayed heat transfer from the heated outer surface. It is of interest whether the induction heating method will be able to dissolve present σ phases during the present time window. Temperatures are high but not held there for long.

3.2.9 Expansion

Expansion occurs after the billet has been heated at the prior stage, then it will be transported (Cooling 2 in Fig 14) into the expansion press. A cone will be pushed through the pilot hole, which was drilled beforehand, and expand the inner diameter. This volume will be deformed, the billet will be elongated and heat will be generated which helps re-crystallization at those areas if the temperature is high enough [25]. When the billet is transported to the second induction furnace its outer surface temperatures can cool down to σ -equilibrium.

For the duration of expansion, including transportation, the temperatures are cooling down close to σ -peak equilibrium, temperatures referring to Fig 9. Together with the time of transportation, it is possible that σ could precipitate or re-precipitate here. The worst cases are for the outer end surface edges of the billet because these cool at higher rates than the rest of the billet.

Additionally, a bar that is not re-crystallized and not σ -free will be much more prone to precipitation at these temperatures. Old grains and local concentrations of Mo and Cr are sensitive to cause precipitation when expanding and transporting the billet. This is why a fully re-crystallized σ -free bar prior to expansion gives the best quality.

3.2.10 Billet induction heating before extrusion (Heating 2)

After expansion, the expanded billet is transported to reheating at a second induction furnace (Heating 2 in Fig 14). Temperatures are set to reach a slight increase in temperature compared to Heating 1. At this stage of heating, there is rarely any cycling because the billet is thinner than before expansion. Therefore the depth of penetration is now sufficient to heat the complete wall of the billet and thus there is less need for cycling. If the billet is held for too long the material may be too hot, especially the inner surface. After temperatures reach the set temperature the billet is taken out immediately.

3.2.11 Extrusion

The hot billet is pressed through a die seen in Fig 17. From the figure, plastic strain can be observed to be large at the opening between the mandrel and the die. Deformation at this scale will re-crystallize grains to a large extent and will be most evident at volumes with the highest deformation. This occurs when the strain is higher than the critical strain for re-crystallization [26]. During steady state, with the deformation that the material experiences, heat will be generated. Increased heat could help the kinetics behind dissolving σ -phase if temperatures before extrusion are close to $T_{\sigma MST}$. On the other hand, large deformation (under re-crystallization temperatures) causes an increase in dislocations and formation of vacancies. Already present precipitates, like the hard σ -phase, could even increase the number of vacancies when the ductile matrix is deformed while the precipitates stay intact. The dislocations increase heterogeneous nucleation while vacancies enhance the diffusion of solid solution atoms and in turn help the growth of precipitates [27]. These mechanics are important to consider if deformation at lower temperature regions occurs where the heat generated isn't high enough to surpass $T_{\sigma MST}$ and is lower than the re-crystallisation temperature (high dislocation density). This could in turn only help the growth of σ -phase.

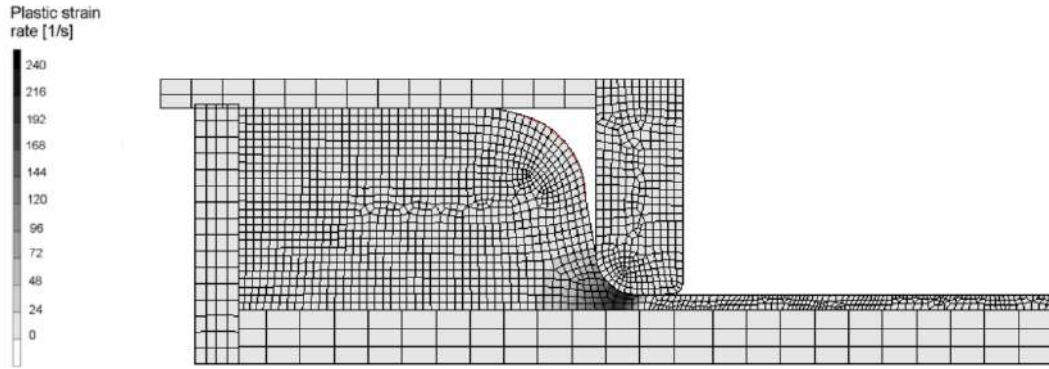


Figure 16: *Heavy deformation seen in a FEM simulation of an extrusion process, illustrated steady state condition* [26]

When the billet is extruded, the front experiences a transient increase in deformation, starting from almost zero at the inner front (referred to as point A in Fig 17), and transitioning towards the steady state (point D and until the back-end of the tube). The transient deformation at the front is depicted in Fig 17, [28].

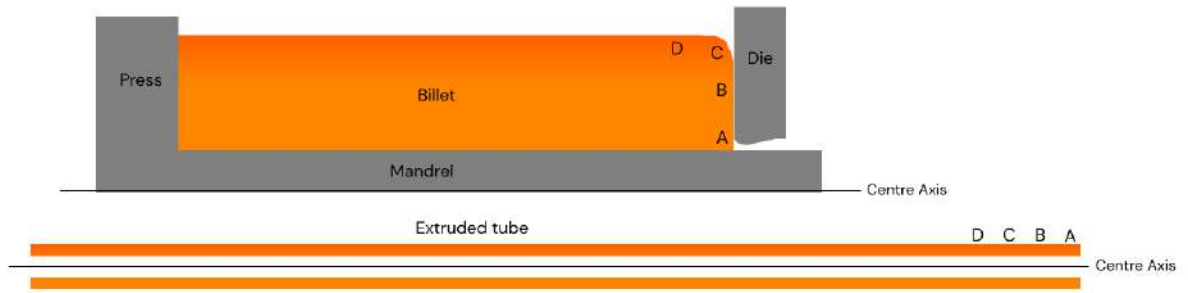


Figure 17: *Simplified illustration of the extrusion process, illustrating the transient stages at the front of an extruded hollow billet from A to D*

3.3 Previous work on Sigma precipitation in Sanicro[®] 28

3.3.1 Development of a dissolution-diagram for sigma in a Sanicro[®] 28 rod

Nylöf et al [20] investigated the relationship between temperature and holding times for dissolving σ -phase in Sanicro[®] 28. If the temperature is above σ -equilibrium, the holding times for dissolution of σ -phases depend on particle size and distribution in the material. If holding times are short, the time of diffusion may be too short and σ won't have time to dissolve, even though the temperature is above or below that of σ equilibrium.

The results in this technical report showed a comparison of the after-forged outer surface (Structure A) and the rod's inner volume (Structure B). The comparison can be seen in Fig [18] and [19].

The different coloured dots of evaluation are:

- green: accepted, σ has been dissolved
- yellow: not accepted: σ has just been dissolved and rest composition can still be seen
- red: not accepted, dissolving has begun but σ is still present. [20]

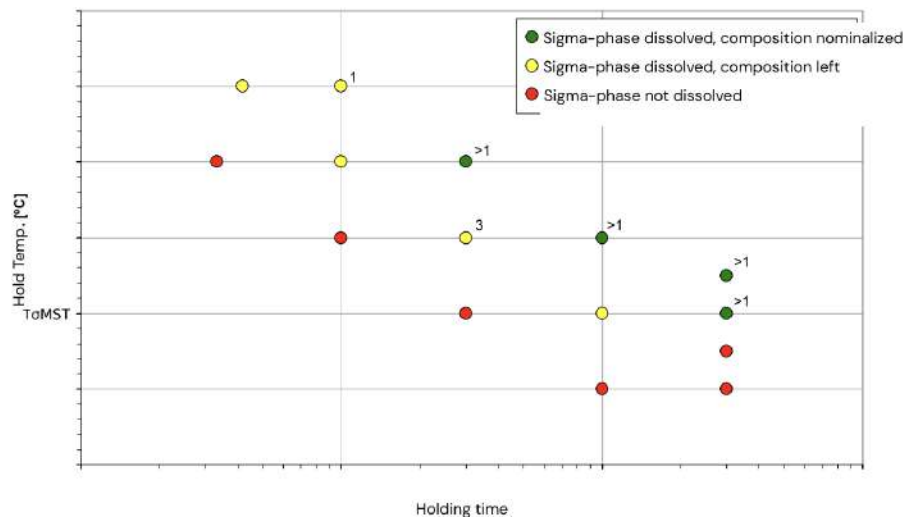


Figure 18: Diagram shows temperature-time (Log) dissolution for structure A, up to 20mm from outer surface [20]

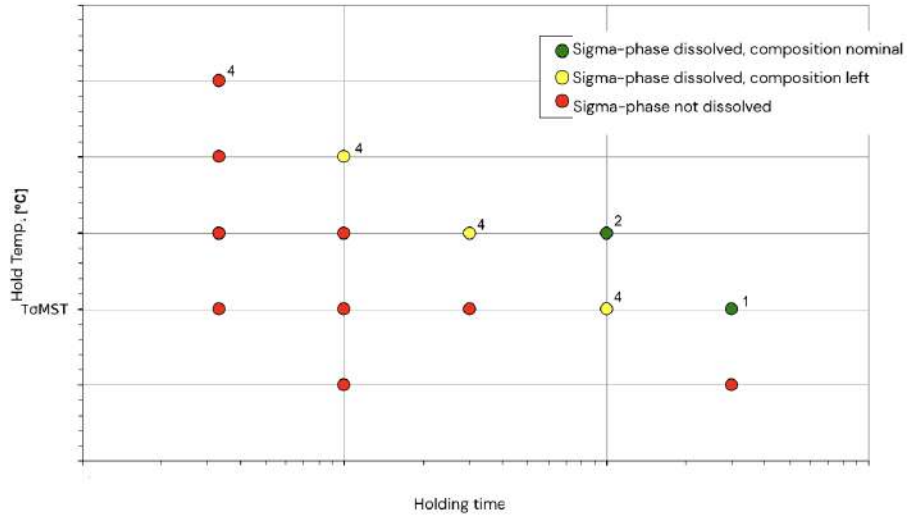


Figure 19: Diagram shows temperature-time (Log) dissolution for structure B, in 45mm and to centre [20]

3.3.2 Documentation of microstructure of an ingot cast San28Cu bar

Pipe-couplings have earlier shown σ precipitation after extrusion and it is proposed that this originates from the forging process. This led to the idea to use a walking beam furnace to quench-anneal the extrusion bar and dissolve all σ . Earlier tests were done on this matter. Some σ was found after quench-annealing with the lower temperature setting (strategy 80), but instead Meurling studied σ precipitation with higher temperature setting (strategy 100) in quench-annealing.

From the technical report made by Meurling [29], the results show σ -phase from strategy 80 in both ends of the bar and mostly at the outer surface down to 100mm deep. At the middle of the bar, more re-crystallization occurs and less σ is found. σ grows between large grains in recrystallized grain boundaries with the largest fraction at the surface. The most probable explanation is that σ is still left from forging and that strategy 80 isn't sufficient enough to dissolve σ .

From the results through strategy 100, the results differ a lot from the previous. At one end, re-crystallization and growth of large grains are found at the outer surface (110mm deep) with σ fully dissolved. σ is found at the inner parts of the bar. At the other end of the bar, no σ was found at all depths from the outer surface. Meurling [29] proposed an explanation as to why one end of the bar contains σ and the other does not. The ends are experiencing different heating and quenching speeds and one end may have been heated/quenched too slowly which led to σ precipitating.

The overall conclusion from this technical report was that most σ precipitates were found at the centre of one end from the bar that was quench-annealed with strategy 100. Though it's important to note that it's preferable if σ precipitates exist at the centre of the bar than at the

outer surface because the billet is later drilled at the centre. Strategy 100 shows from this report no σ at the outer surface which is the best option in this case. [29]

3.3.3 TTP-diagram for Sanicro[®] 28

To understand the nucleation and growth of precipitates, Nylöf wrote a technical report on temperature–time precipitation for a Sanicro[®] 28 bar, producing a Time Temperature Precipitation (TTP) diagram. The bar is free from σ before conducting these tests, solution heat treated and then immediately applied testing temperature.

The results showed growth of two intermetallic phases, σ and a chromium-nitride phase with lower Cr and Mo than that of σ , after long holding times. [30]

3.3.4 Precipitation Kinetics of Sigma Phase during Extrusion of San28Cu tubes

Even though a lot of work already has been done regarding σ precipitation in Sanicro[®] 28, it could still be found in extruded tubes. Kolmskog [19] studied the effect of σ precipitation during extrusion and cooling through Gleeble Thermal-Mechanical Simulator (GTMS). The technical report indicates that cooling rates does not affect σ precipitation by any means. Later the temperature was decreased to simulate insufficient heating. σ was now found even though Kolmskog refers maximum σ stability at lower than this second temperature. The heating is just above stability and wouldn't be able to dissolve already present σ . Conclusions are that it's important that the temperature at billet heating before extrusion is slightly over $T_{\sigma MST}$, as well as the focus should be directed at heating processes instead of cooling in order to reduce σ -phase fraction. Macro segregations were found to affect small variations in σ precipitation. An increase of 0.4% from the nominal composition was found at local areas (3.29%->3.77%), causing an increase of $T_{\sigma MST}$ to 30C higher. Local peaks could increase this number even further. These segregations often occur towards the centre of the bar which has been concluded to not drastically interfere with the product because the material is drilled away at pilot-hole drilling.

4 Method

The experiments made can be divided into two areas of heat treatment processes. A simulation of induction furnace heating in expansion/extrusion and the other, re-heating in a CWF after forging. The induction heating is made into three sections, Heating 1 (first induction furnace and cooling to second induction furnace), Heating 1 stop scenario and a simulation of soaking.

4.1 Material

To illustrate all samples and their radial location, Fig 20 is presented. All samples are taken and run as doubles.

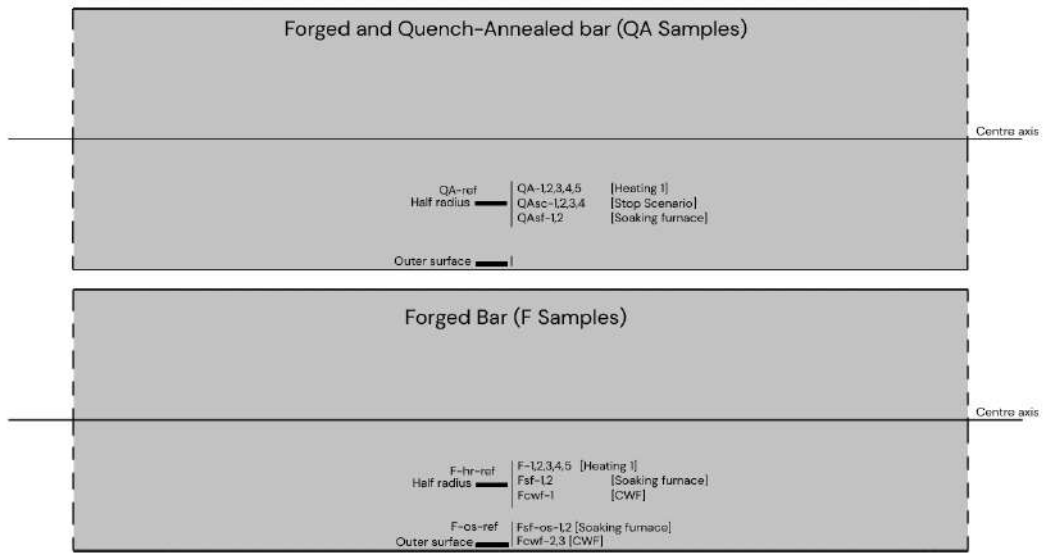


Figure 20: Illustration of where samples are taken from a bar

4.1.1 Quench-annealed samples

Samples are cut from an in-process bar (charge 558340) of $\varnothing 324\text{mm}$ that has been put through the complete process until after quench-annealing. The samples are taken from the half radius at a random axial location of one bar with the length of the rod in the direction of the bar's length. These are cut into $11 \times 11 \times 120\text{mm}$ rods and are marked as Quench-Annealed QA-nr, additionally, one reference sample is marked as QAref, shown in Fig 21. QAref, sampled from half radius, was free of σ and had very large re-crystallized grains. Note that QA samples also have been forged before quench-annealing but are marked only QA as to indicate the last heat treatment process. The chemical composition of the QA samples is shown in table 2.

Samples	C	Si	Mn	P	S	Cr	Ni	Mo	Cu	N
Nominal	≤ 0.020	≤ 0.7	≤ 2.0	≤ 0.020	≤ 0.010	27	31	3.5	1.0	≤ 0.1
QA	0.009	0.43	1.66	0.019	0.001	27.07	30.77	3.28	0.91	0.068

Table 2: Chemical composition QA samples



Figure 21: *LOM Image (100x) shows QAref, reference sample taken at half radius from a quench-annealed bar, grain size ASTM 0*

4.1.2 Forged samples

A forged bar is quenched down to room temperature and then sampled at two different locations from the same bar (charge 567792). At half the radius and at 20mm from the outer surface. The rods are cut similarly to the QA samples. The reference sample F-hr-ref cut from the half radius location is shown in Fig 22. The reference sample F-os-ref, for the outer surface of the forged bar, is shown in Fig 23. The chemical composition of F samples is shown in table 3.

Samples	C	Si	Mn	P	S	Cr	Ni	Mo	Cu	N
Nominal	≤0.020	≤0.7	≤2.0	≤0.020	≤0.010	27	31	3.5	1.0	≤0.1
F	0.008	0.40	1.84	0.018	0.001	26.68	30.61	3.31	0.93	0.059

Table 3: Chemical composition of Forged samples

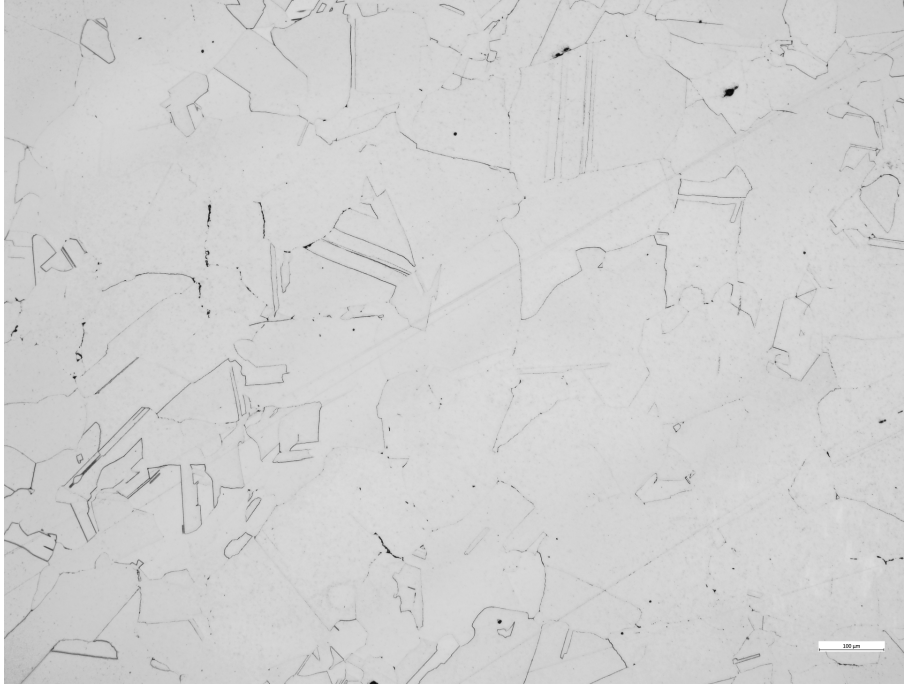


Figure 22: *LOM Image (100x) shows, F-hr-ref, reference sample taken at half-radius in a forged bar, small amounts of σ -phase is present, grain size ASTM 4.0*

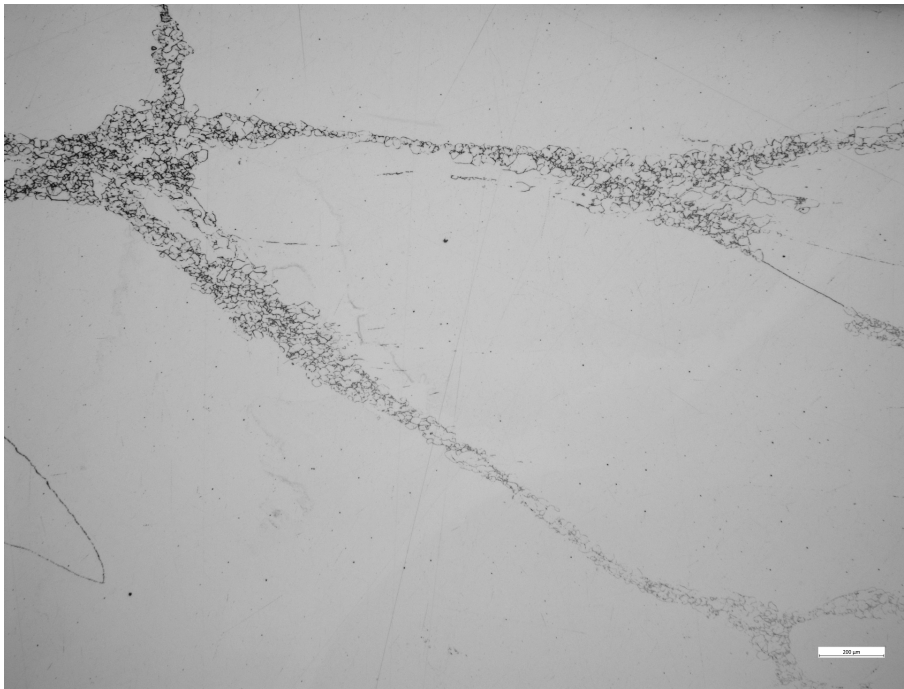


Figure 23: *LOM Image (50x magn) shows reference sample F-os-ref, with necklace structure, taken at outer surface from a forged bar, σ -phase is present between the large grains*

4.2 Experimental procedure

Heat treatment experiments were conducted in a Gleeble 3500 Thermal Mechanical Simulator, a tool that provides temperature to time as well as mechanical strain and elongation in a controlled

system. Samples were put into the simulator and were prepared beforehand with welding to attach the electric wire. Temperature is then generated by the current and the sample is cooled by conduction from the copper fixtures, which are cooled by 14°C water. The setup is seen in Fig 24

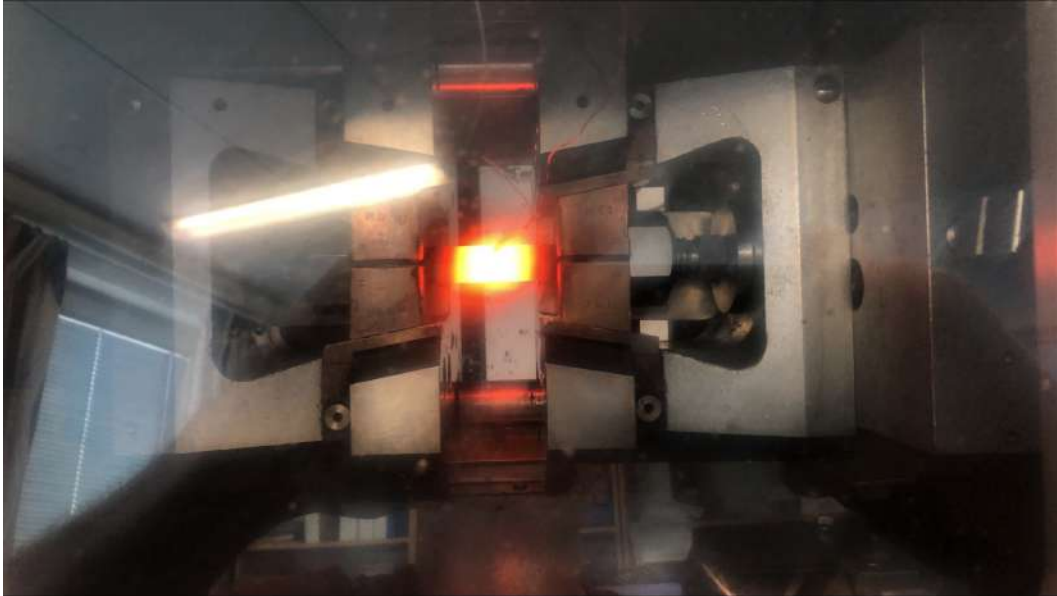


Figure 24: *Gleeble thermal experiment heating up a rod sample, observed wire and copper fixtures, together with heated rod*

4.2.1 Gleeble Heating 1 induction furnace experiments

The experiment is conducted as follows. The sample is heated to a varied top temperature, held for the duration of cycling and then cooled down with a constant cooling rate for a varied time. After it's been held for the varied time the sample is cooled with cooling rates (120°C/min) representative to quenching down to room temperature, as seen in Fig 12. The Gleeble heating curve for this experiment is designed without consideration of temperature increment from deforming the alloy when the hollow billet is expanded. The heat generated at the expansion procedure is instead generalized as a constant cooling rate in air for the duration of the expansion.

Quench-annealed and forged samples are made parallel to one another, meaning the same temperature-time in a Gleeble run for example QA-1 and F1 is used. The attempts and their temperature-time curves are compiled in Fig 25

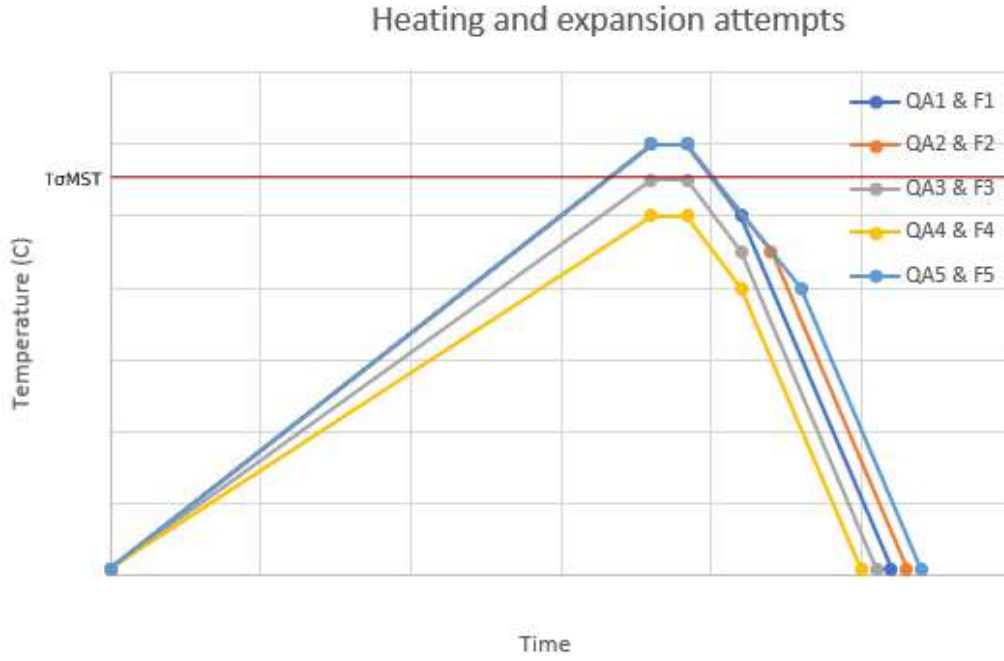


Figure 25: *Temperature-Time experiment curves of heating and expansion, one colour indicates one Gleeble run for QA and F*

4.2.2 Gleeble Heating 1 stop scenario experiment

A simulation of a stop in production at the first induction furnace was also made. Here the temperature curve is set to simulate a stop to observe if a stop will cause σ -precipitation. The sample is then both quenched and continued heated as in Heating 2, where it's held and then quenched. The attempts and their temperature-time curves are compiled in Fig 25

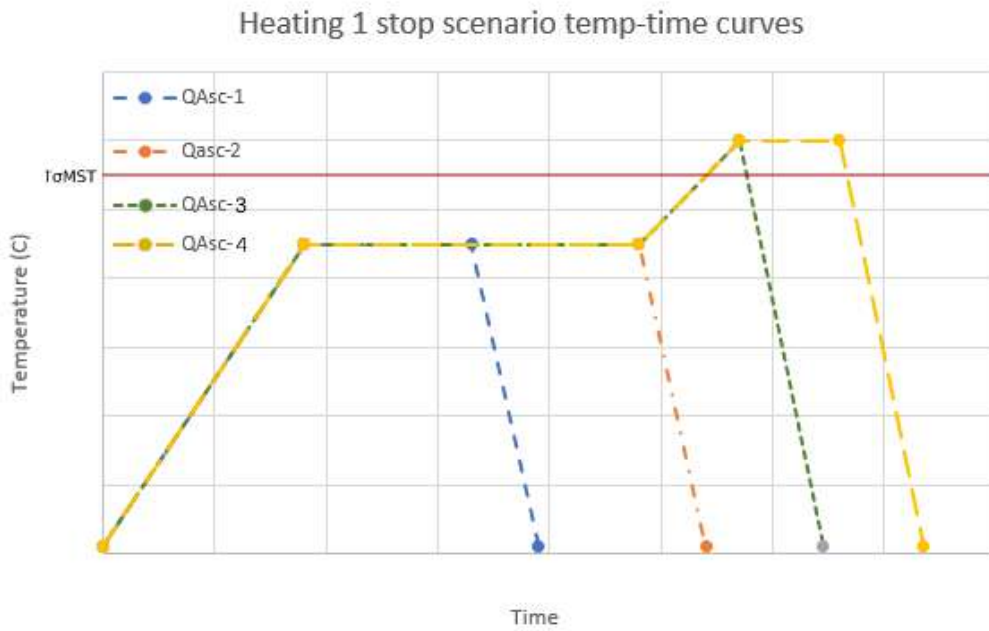


Figure 26: *Temperature-Time experiment curves of a stop scenario at 900°C in induction furnace 1*

4.2.3 Gleeble soaking experiment

A "full run" experiment was made to simulate a hypothetical scenario where σ will precipitate at Heating 1 with insufficient heating plus a stop scenario and then made to be dissolved with soaking. The idea is to force σ in a "worst case scenario" and then see if soaking is enough to dissolve precipitates. A comparison between a forged (half radius and outer surface) and a quench-annealed σ free sample is made and quenched before and after the Heating 2 plus soaking. The attempts and their temperature-time curves are compiled in Fig 27

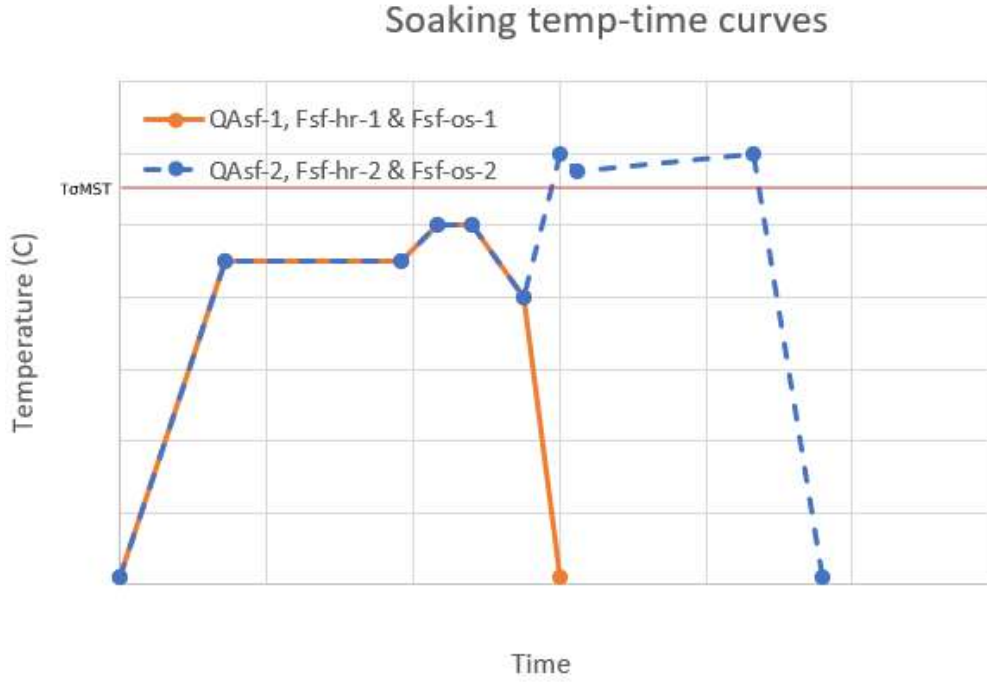


Figure 27: *Temperature-Time experiment curves of the soaking simulation*

4.3 Re-heating in CWF after forging experiments

4.3.1 Computed simulation of reheating in CWF

A Finite Element Method simulation of local temperature change in a forged bar of dimensions 334mm was made. The events are the following: homogenous start temperature -> forged (air cooled)-> cooled in air (transport) -> reheated with CWF -> cooled in air (transport)-> quenched. 5 temperature points are measured. At the mid-centre, half-radius, outer mid surface, outer end surface and upper end centre.

4.4 Gleeble Reheating CWF experiment

The reheating in CWF experiments are conducted using similar temperature-time curves that were brought forward in the computed simulation. These curves are fit to match the simulated theoretical values as closely as possible to mimic the reheating of the forged bar. Three locations of a forged bar are inspected and taken as samples, half radius (Fcwf-1), mid surface (Fcwf-2)

and outer end surface (Fcwf-3). References for the samples are seen in Fig 22 for the half radius and Fig 23 for the surface.

4.5 Sample preparation

After the samples have been heat-treated using the Gleeble 3500 they are cut into 11x11x15mm samples and sampled from the middle of the heat treated 11x11x120mm rod. When cut, the samples are marked with an X to indicate what side will be analysed by optical microscopy. In these cases all samples will be observed at a surface tangent to the longitudinal direction of the in-process bar. It is unknown in what direction the surface is normal to.

When samples have been cut they are cast into regular polymer billets and polished according to the material polish recipe. When ready, samples are etched using oxalic acid solution for either 10 seconds or one minute. Common practice when looking for σ in Sanicro[®] 28 is to first etch for a short period to only highlight precipitates. However, for a grain size estimation, one minute with higher voltage is required in order to highlight all grain boundaries.

4.6 LOM

Samples are first analysed using Light Optical Microscopy (LOM) which will tell whether or not signs of σ is present in the observed sample. Later, the sample can be etched further to observe grain sizes. Estimation of grain sizes can be done using LOM by using a software tool that lets the user manually add points, indicating grain boundaries, on intercept lines. Samples of interest are measured using this tool and are provided in the results.

4.7 SEM/EDX

To conclude observations in LOM, Scanning Electron Microscopy (SEM) equipped with Energy Dispersive x-ray spectroscopy (EDX) was used for samples of interest. σ is a Cr- and Mo-rich precipitate which are heavy elements, thus this will show as bright strokes/dots in SEM. EDX was then used to confirm sightings in SEM with elemental composition.

5 Results

5.1 Simulation of Re-heating in a Car-wagon furnace

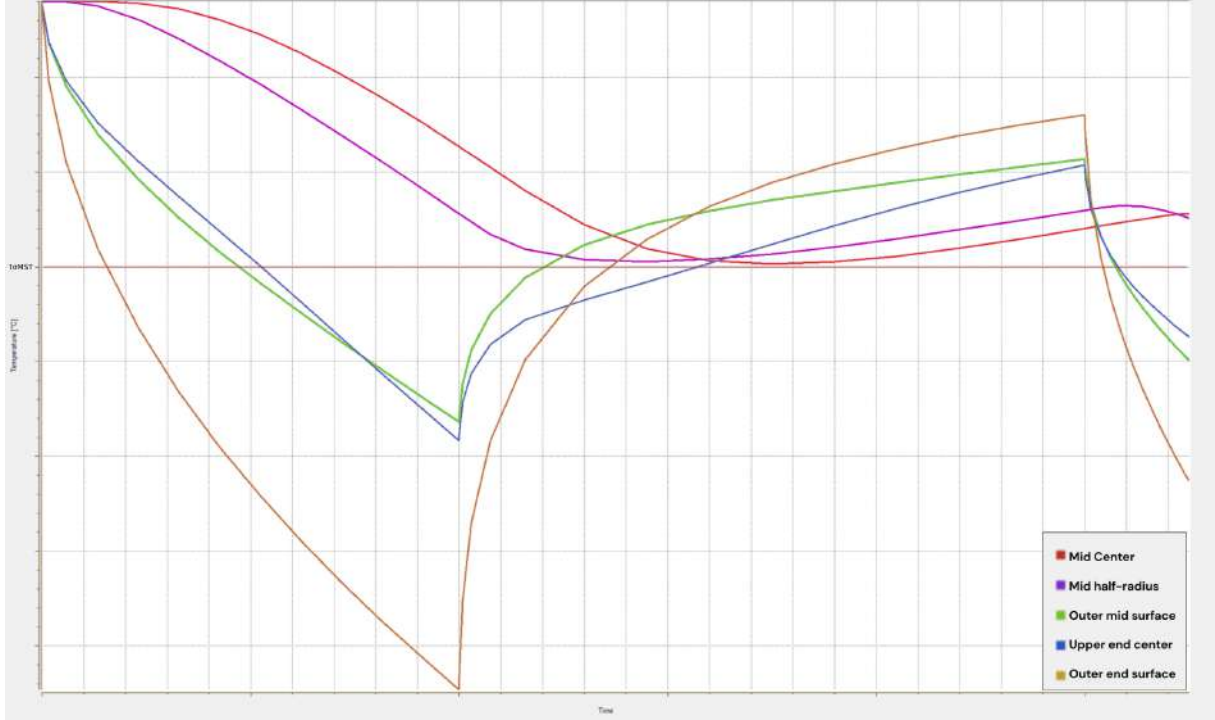


Figure 28: *Temperature run; air-cooling 20 min (forging), re-heating 30 min (CWF) and air-cooling 1 min (transportation to quenching)*

Air-cooling and reheating was simulated using the Finite Element Method and the results can be seen in Fig 28. The figure shows temperature change at five positions on a simulated forged bar with re-heating in a CWF. The first section is the air cooling at forging (without simulated deformation). The temperature is then raised when the bar is put into the CWF. The inner volume (red and purple lines) of the bar shows a large difference in cooling rates compared to the surface points (orange, blue and green). The increment in temperature can be seen right as the bar is put into the furnace for the surface while the inner volume will be delayed due to temperature gradients. The inner volume can also be seen not to fall below $T_{\sigma MST}$, at any time of the forging + re-heating process.

The surface points show a decrease in heating rates as temperature increases. Time to heat up the surface over $T_{\sigma MST}$ is however quicker. After this, temperatures are above $T_{\sigma MST}$ for a sufficient enough to dissolve σ -phase. However, the outer end surface (orange) curve is the only curve that is high enough for a prolonged time that is enough to dissolve σ at faster rates.

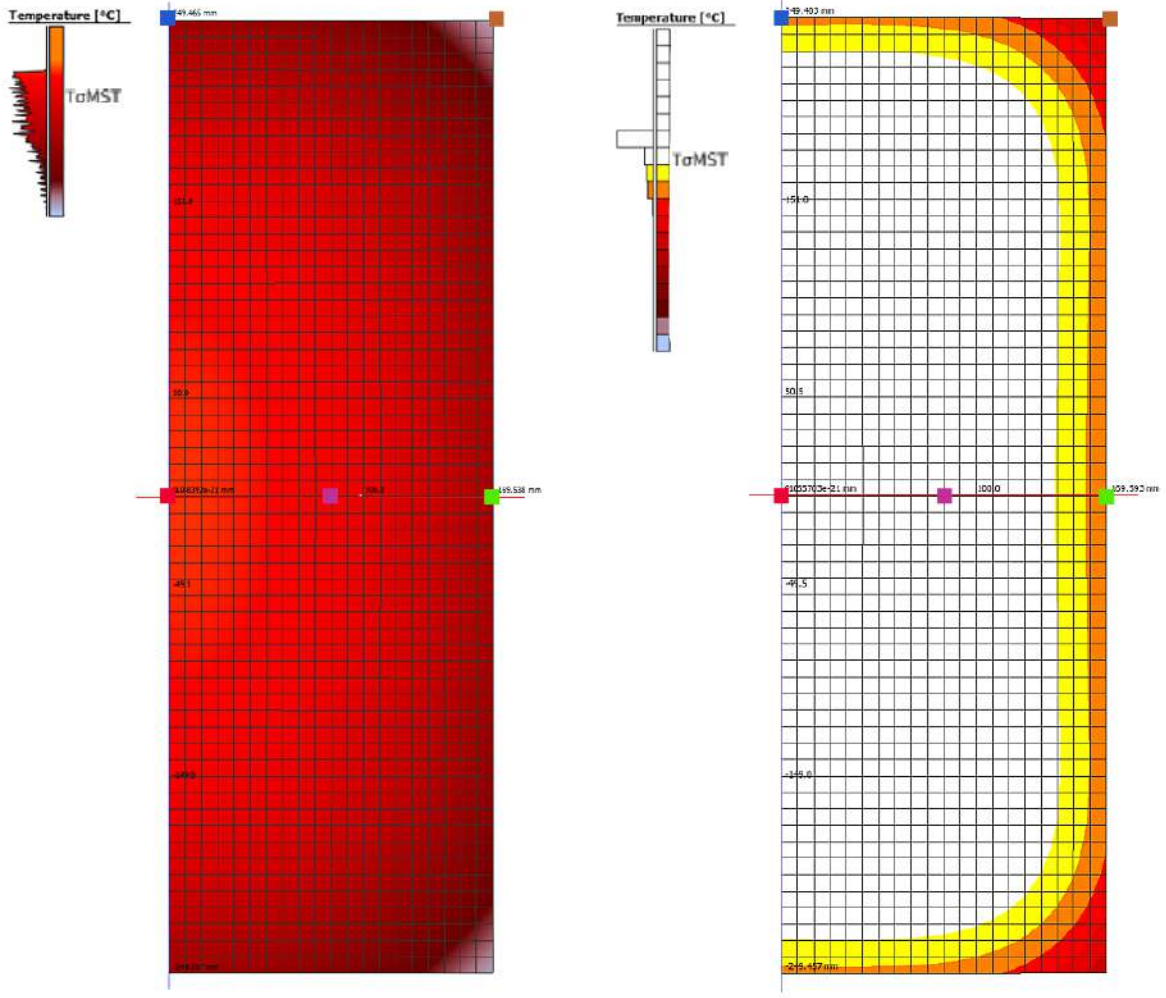


Figure 29: Temperature half profiles of the forged bar from centre axis to outer radius, left shows profile after forging and right shows profile after CWF Fig 28

The temperature profiles of the forged and re-heated bar are shown in Fig 29. The left profile indicates the scenario where quenching is carried out right after forging. Most of the profile is well below $T_{\sigma MST}$ at the surface ends. The profile to the right shows the temperature profile right before quenching after re-heating. The time for transportation, after the CWF, to quenching is simulated to 5 minutes, although it may well be under one minute. Coloured areas are areas that will be below $T_{\sigma MST}$ when quenched. However, temperatures here are well above temperatures compared to the left profile and will only be under $T_{\sigma MST}$ for a short period, see Fig 28.

5.2 Analysis of Gleeble CWF experiment

Initially, the half radius and surface reference samples show irregular and deformed microstructure, this can be observed in Fig 22 and 23 respectively. All of the samples after being run in the simulated CWF in Gleeble, showed re-crystallization throughout the samples, even the very large grains that are present at the surface in the necklace structure. The time above $T_{\sigma MST}$ is enough to dissolve all σ precipitates that were present before reheating. This was observed in both LOM and SEM. However, for sample Fcwf-1, indications of σ could be found in the form

of thinner strokes of dots, as can be seen in Fig 30, but were not found in SEM. Thin strokes of dots like this could indicate that they are Cr-carbides, as was found in another sample QAsc2 in SEM/EDX.



Figure 30: *Observed Fcwf-1 in LOM at 100x magnitude*

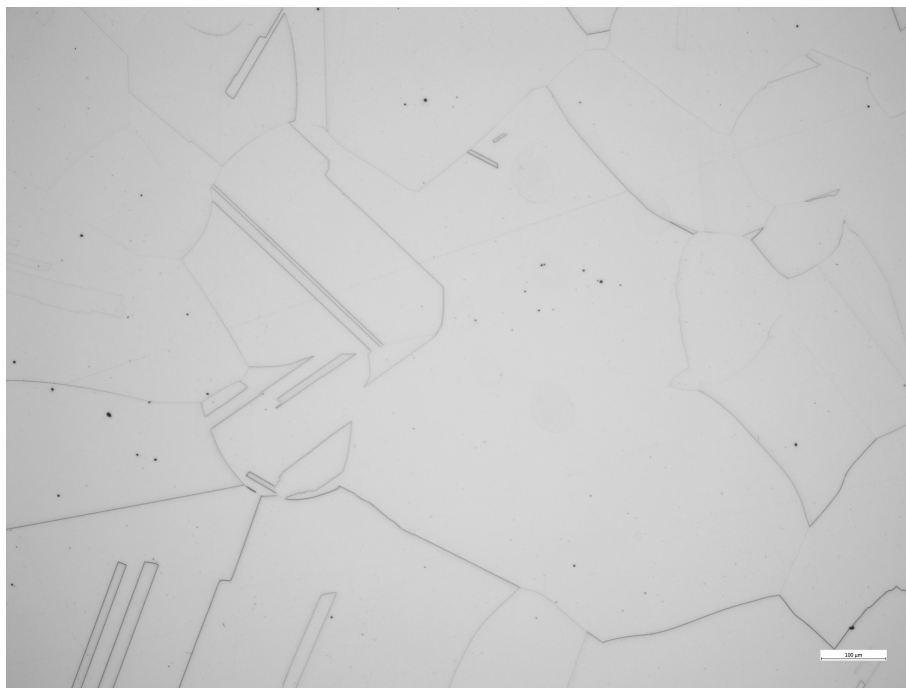


Figure 31: *Observed Fcwf-2 in LOM at 100x magnitude*

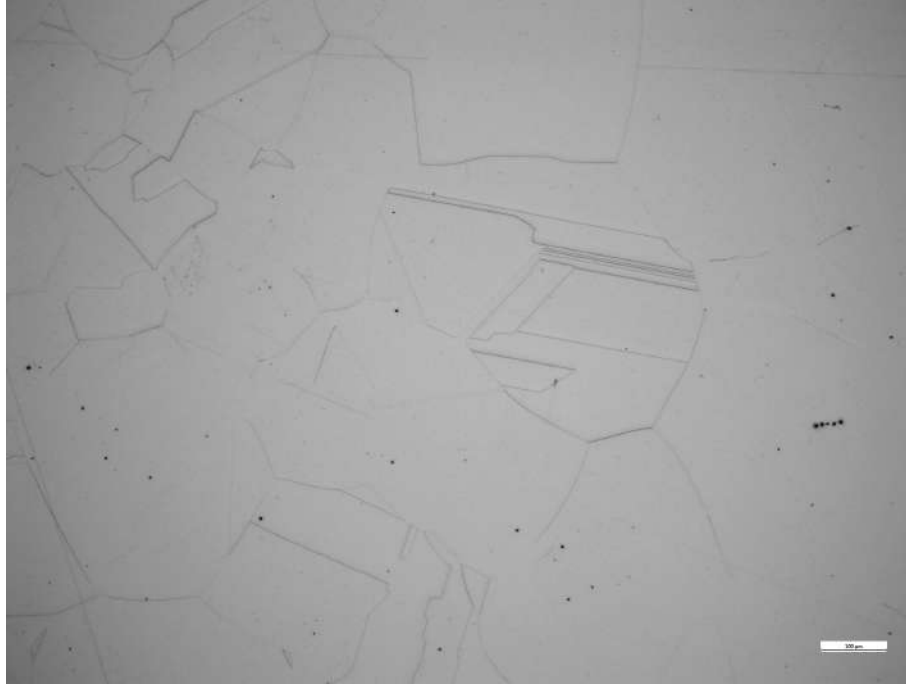


Figure 32: *Observed Fcwf-3 in LOM at 100x magnitude*

Grain sizes are different to their respective reference sample. At half radius, sample Fcwf-1 have grown to around size 2.0 from 4.0. At the surface samples (Fcwf 2 & 3), much larger grains are found at size 1.0. The very large grains in the necklace structure have re-crystallized and instead grains of size 1.0 are present. The scale of the reference sample grains are much larger than the largest size 0 in ASTM measurement.

A difference in grain sizes after CWF is 2.0 at half radius to 1.0 at the surface. This comparison can be seen more clearly in SEM in Fig [33](#). Sample Fcwf-3 was not scanned in SEM but Fcwf-2 can be comparable as grain sizes were measured equal in LOM.

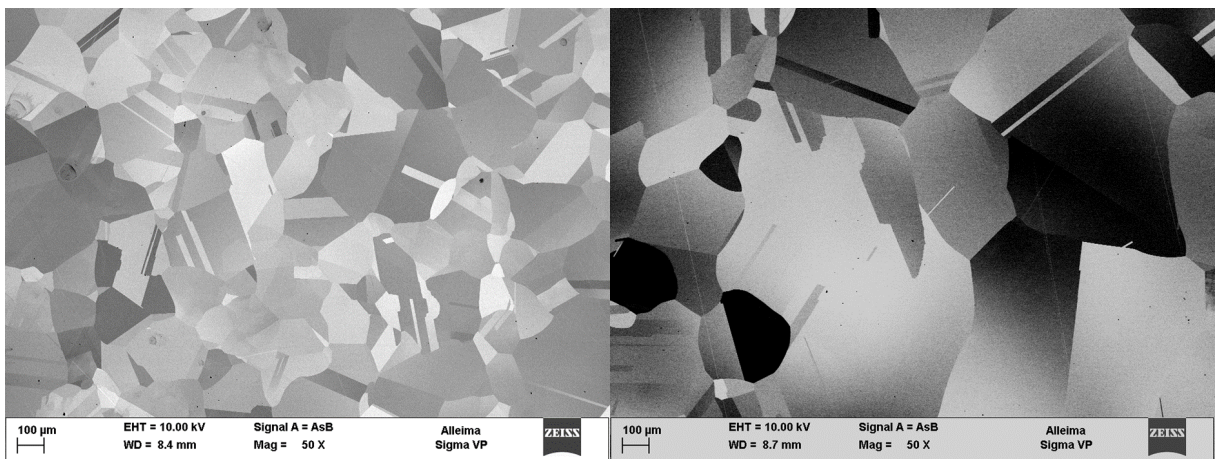


Figure 33: *SEM image at 50x magnitude, shows Fcwf-1 (left) and Fcwf-2 (right) difference in grain size 2.0 and 1.0 respectively*

5.3 Analysis of Expansion/Extrusion experiments

The results of Heating 1 experiments are summarized in Fig 34.

Expansion	Sample nr	σ state a	σ state b
QA Samples	QAref		
	QA-1		
	QA-2	SEM	
	QA-3		SEM
	QA-4	SEM+EDS	BSSEM
	QA-5	SEM	
F Samples	Fref		
	F1		
	F2		
	F3		
	F4		
	F5	SEM	

Figure 34: Observed σ in Heating 1 experiments

Observations that can be seen are that samples that have reached Heating 1 top temperature do not contain precipitates. For the F samples, the time at this temperature is also long enough to dissolve any σ that was present. This was found when comparing Fref to F1, F2 and F5. σ is present to a small extent in Fref but is dissolved in F1, F2 and F5. All samples that were free of σ , QAref, QA1, QA2, QA5, F1, F2 and F5, were observed in LOM and showed only faint, sharp grain boundaries without any darker irregular lines or strokes of dots, Fig 35 for sample QA5. Note that the samples are intentionally etched to only show precipitates, thus why it is difficult to see grain boundaries in samples without precipitates.

Additionally, samples 1,2 and 5 showed no difference in σ content, indicating that cooling to different temperatures does not affect precipitation.

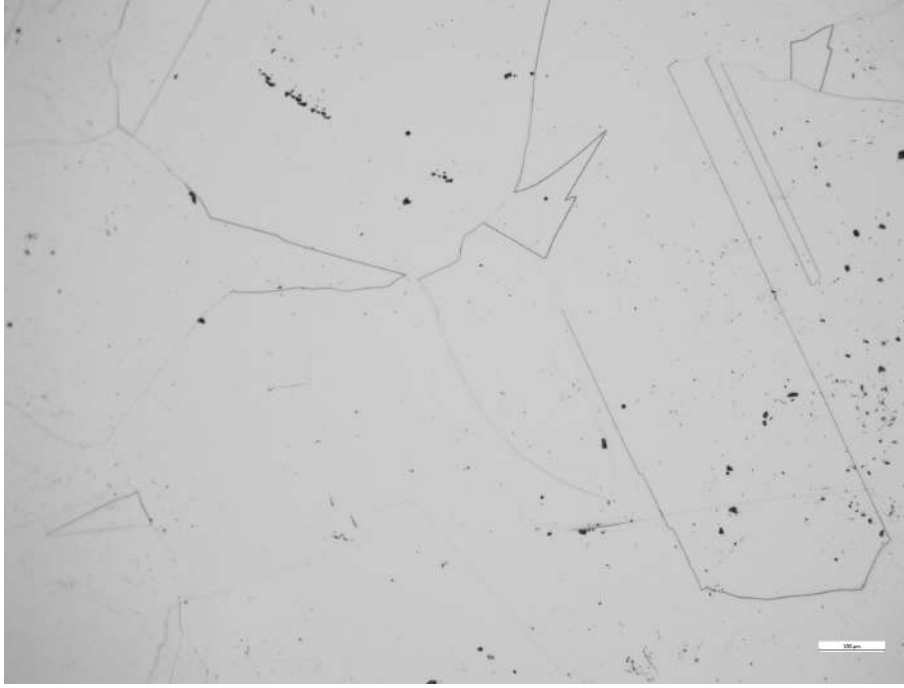


Figure 35: *LOM 100x magn; σ -free sample QA5 shows faint grain boundaries without any signs of σ , black dots are either oxides or external particles not relevant for the case*

Temperatures equal to and below $T_{\sigma MST}$ were found to induce σ precipitation at different levels. Samples QA- 3 & 4 and F- 3 & 4 all contain more precipitates than their respective reference sample, compare to Fig [21](#) & [22](#) respectively. In Fig [36c](#) σ can be seen as dark continuous irregular strokes in grain boundaries. Note that faint, sharp lines can be seen, which are twin boundaries where precipitation rarely occurs.

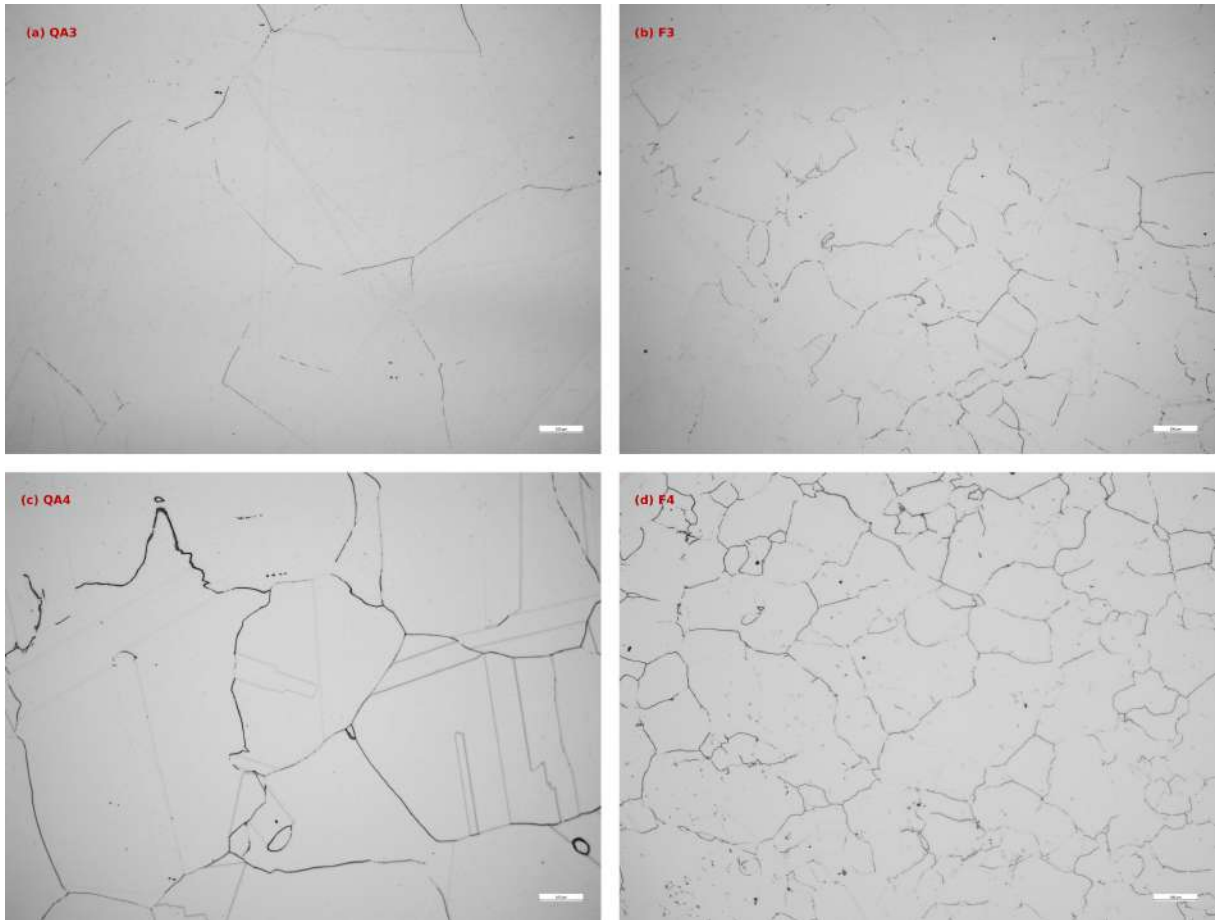


Figure 36: Images shows LOM 100x magn analysis of sample QA4, dark irregular lines are most likely σ -phase, twin boundaries can be seen in grains as faint lines

The differences in the amount of σ are shown as variety in lines. An observation that can be made from the difference between QA3 and QA4 are that lines are continuous to a larger extent in QA4. QA3 shows thinner irregular lines and more dots continuing from triple junctions and can be seen in Fig 37. To interpret the volume fraction of σ is difficult to do from LOM alone but it can be said that more growth of σ has occurred in QA4 compared to QA3. Because the same temperature curve is used for F3 and F4 respectively, the same can be said for F4 compared to F3.



Figure 37: LOM (200x magn) image of area in Fig 36a showing discontinuous dotted lines in a triple junction in sample QA3

5.3.1 SEM & EDS analysis for Heating 1 experiments

SEM analysis was made at the same area as Fig 36c and can be observed in Fig 38. In SEM, σ is seen as white dots or lines in grain boundaries. White strokes and dots was found in both QA-, F-, 3 and 4, although to a smaller extent in samples 3 than 4.

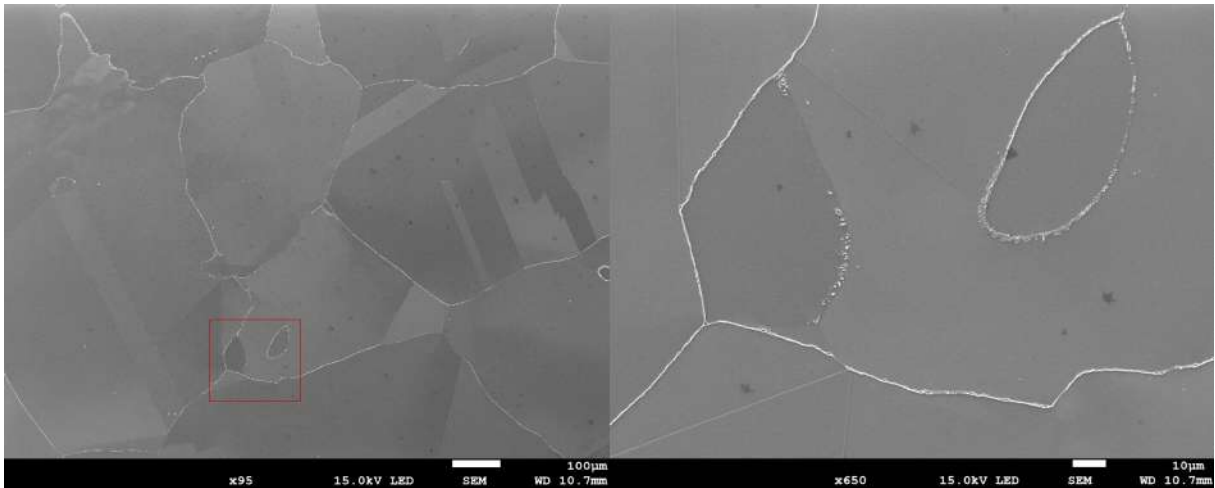


Figure 38: SEM image of area in Fig 36c, shows precipitates in grain boundaries, white lines indicates σ -phase

SEM equipped with EDS highlights the observed σ -phase observed in Fig 39 & 40. The black blob was confirmed to be an inclusion with both Aluminium- (Al) and Magnesium- (Mg) oxides. EDS analysis shows that the white shape precipitates contain a large amount of Mo (8.8%) and

Cr (40%), as well as less Fe and Ni, which are indicative of σ -phase.

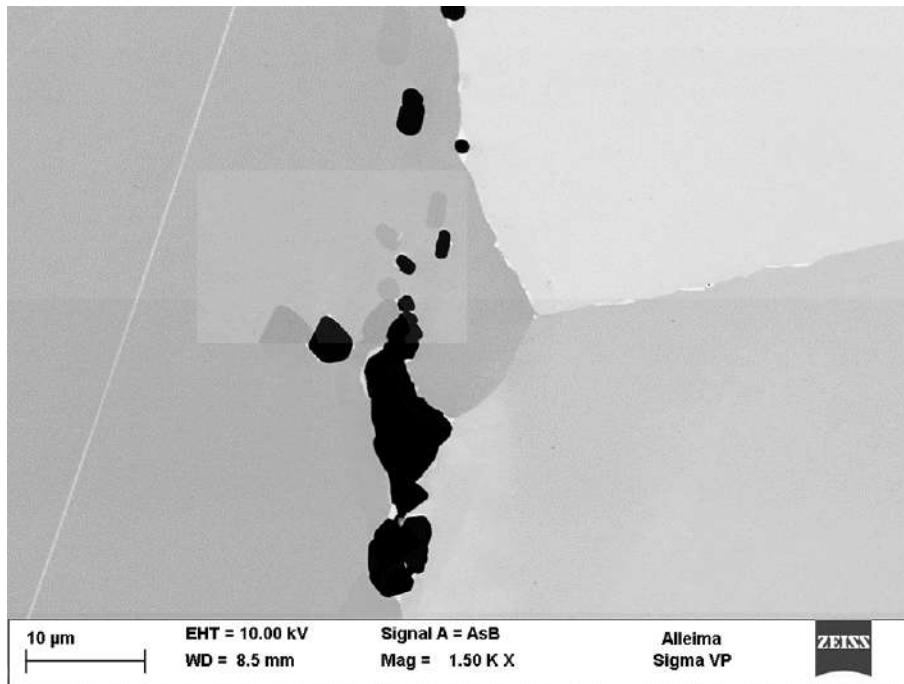


Figure 39: Backscatter mode, SEM image (1500x magn) shows large inclusion of Al- & Mg-oxides, and small precipitates in grain boundaries at the triple junction, white small dots in grain boundaries indicate σ -phase

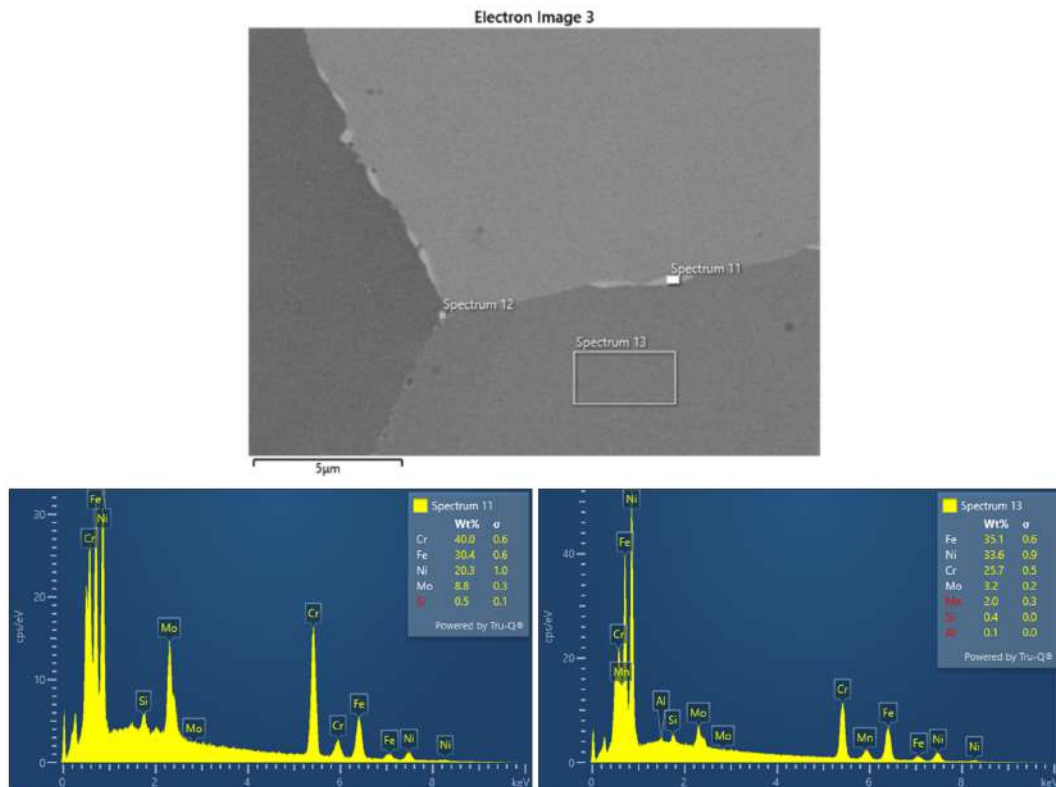


Figure 40: SEM (6000x) & EDS analysis of triple junction in Fig 39, white dots are σ -phase (spectrum 11) in grain boundaries, spectrum 13 maps the surrounding grains, note the small scale/high magnification (6000x) in the electron image

5.3.2 Analysis of Heating 1 stop scenario

The results of the stop scenario can be observed in Fig 41. σ -phase is seen in QAsc-1 and QAsc-2 as both continuous and discontinuous lines. It is then dissolved, right after the temperatures again reach Heating 1 top temperature, seen both in QAsc-3 and QAsc-4. Sample QAsc- 2 and 3 were both analysed later in SEM and showed that sample QAsc3 showed that σ was present, shown in Fig 42. It is not hypothesised that the time here would be sufficient to dissolve the sigma phase. This will be discussed in section 6.3.

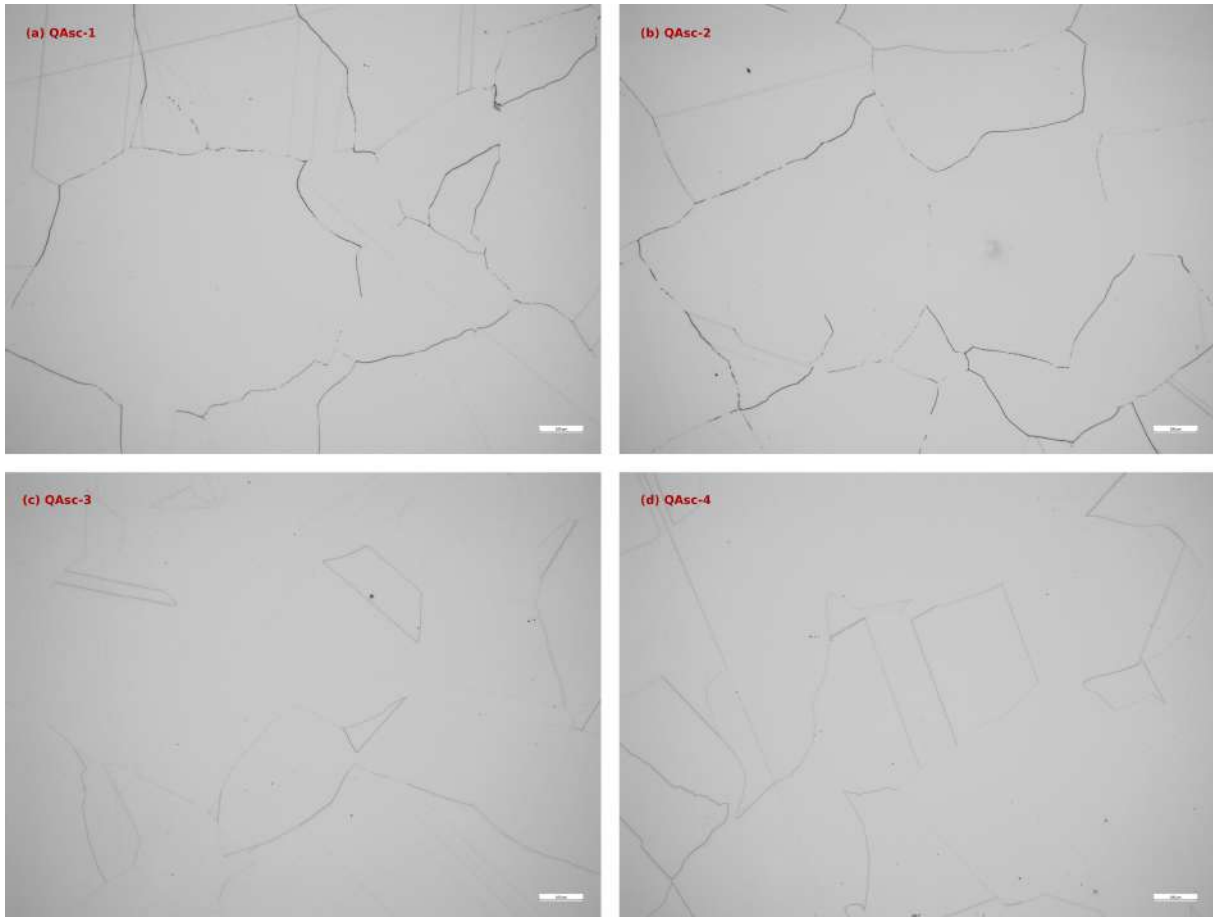


Figure 41: LOM magn 100x shows a) QAsc-1 b) QAsc-2 c) QAsc-3 d) QAsc-4

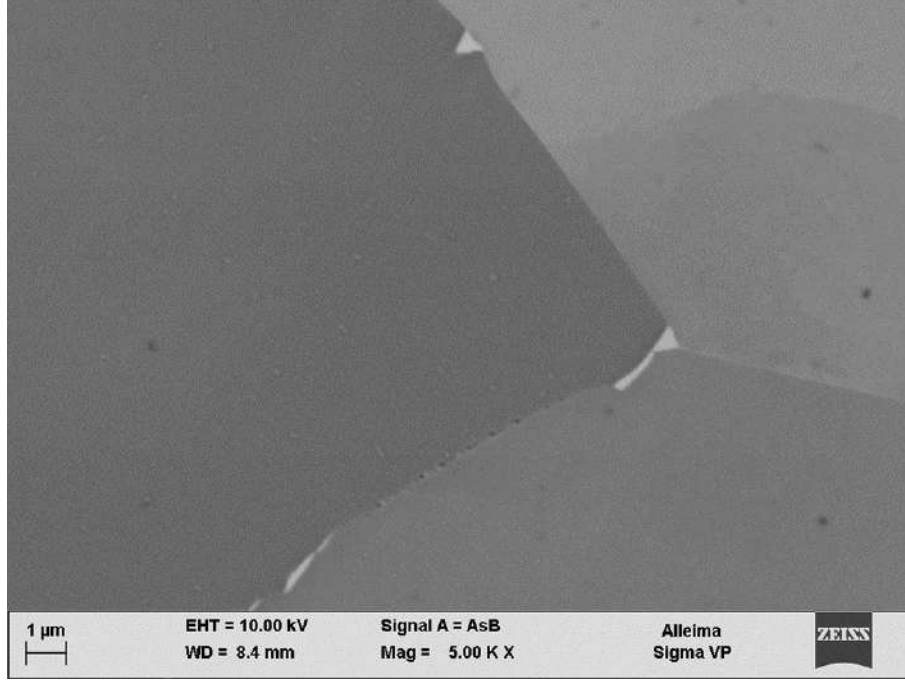


Figure 42: Backscatter mode, SEM image (5000x magn) shows white small dots in grain boundaries that indicate σ -phase

5.3.3 Analysis of soaking experiments

These results resemble the effect of soaking after Heating 2. The results showed no σ in either of the samples (QAsf-2, Fsf-hr-2 & Fsf-os-2) after the soaking. Confirmed through both LOM and SEM. Measured sizes are ASTM 00 for QAsf-2, ASTM 1.0 for Fsf-hr-2 and ASTM 0 for Fsf-os-2. The samples before, QAsf-1 Fsf-hr-1 & Fsf-os-1 in Fig 43a, c & e respectively, have dark irregular lines (σ -phase) in the grain boundaries. That σ -phase is present is intended, as both of these samples endure the imaginary worst-case scenario of a stop and insufficient heating. It shows that soaking is capable of generating the σ -free structure independent of the previous structure.

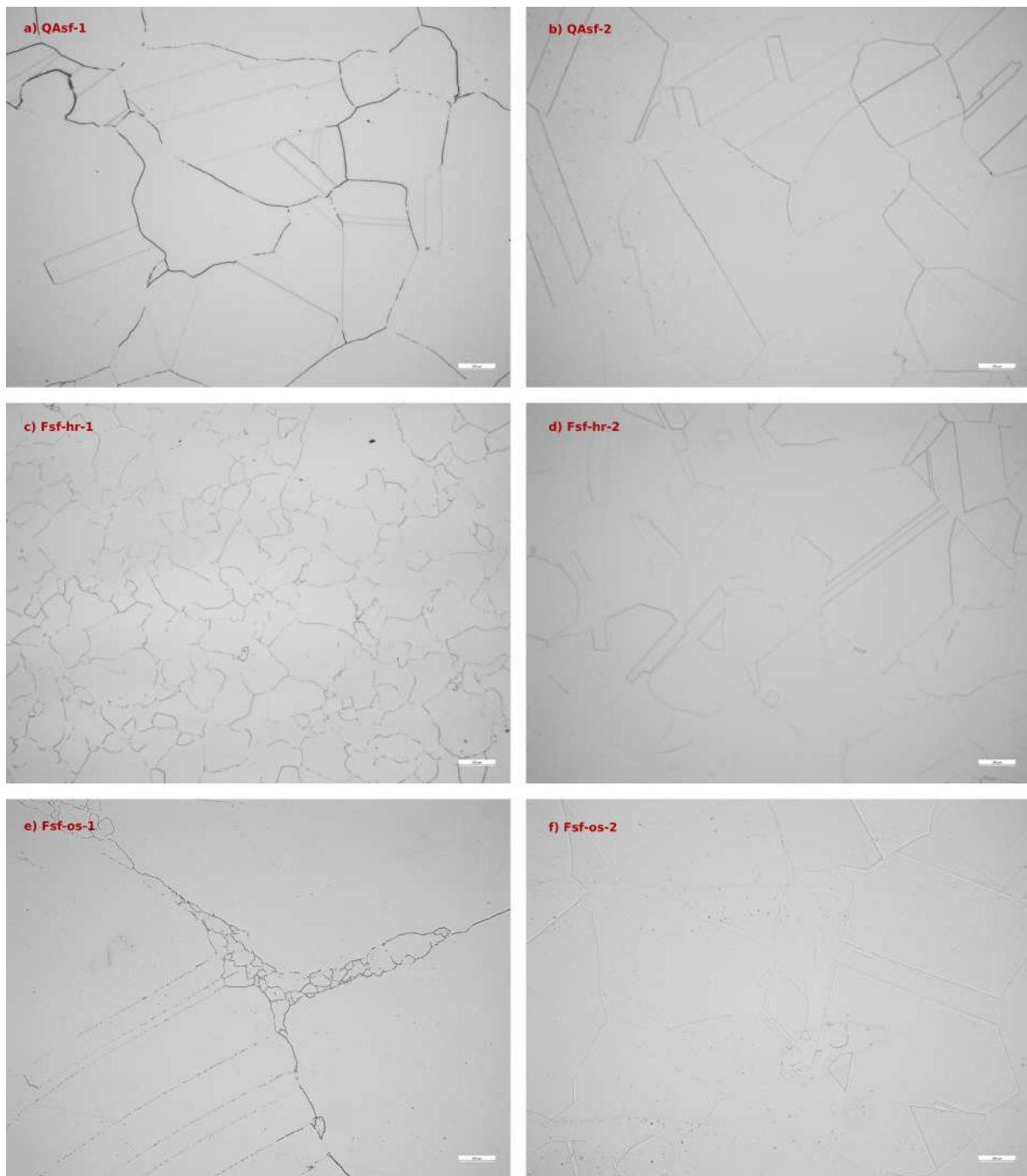


Figure 43: *LOM magnitude 100x shows a) QAsf-1 b) QAsf-2 c) Fsf-hr-1 (half-radius sample) d) Fsf-hr-2 (half-radius sample) e) Fsf-os-1 (outer surface sample) f) Fsf-os-2 (outer surface sample)*

6 Discussion

6.1 Samples

Samples taken from a bar are not taken with consideration of axial location. This means it is unknown if a sample set is sampled from the front, middle or back of a bar. However, all samples, QA and F, are taken from the same respective axial location in their respective charge. Now it makes sense to take the samples in a consistent manner but axial location could affect the results. It has been mentioned earlier that macro segregation could affect the kinetics of σ -precipitation by increasing or decreasing $T_{\sigma MST}$, see Fig 10 again. If $T_{\sigma MST}$ is on the "negative side" meaning if Mo content is low there could be scenarios where those results wouldn't compare to results taken from a high Mo content sample set. A high Mo content, say 4.0%, sample set would be more difficult to dissolve σ . The Mo content in QA and F samples are 3.28 and 3.31 % respectively, which is close to the nominal composition of 3.5, although lower but can be considered representative for a Sanicro[®] 28 bar.

The ideal scenario would be to sample from many charges and chosen axial location. Although, this would be very time-consuming.

The latter also applies to the number of samples taken as doubles. Two was chosen for this project and is not the ideal number, three would be optimal if variation occurs between two samples. Time available in the project was not enough for a triple sample set.

6.2 Deformation

In Fig 28 the temperature profile at the mid-half radius during forging does not fall below $T_{\sigma MST}$. The theoretical values in this simulation, therefore, indicate that σ won't precipitate at this location of a bar. The reference sample Fref from the forged bar is in the same location as this simulation indicates. Here, the theory doesn't meet practice because σ is found in the Fref sample to a small extent. One explanation could be that the simulation was used with slightly incorrect property values for convection, conduction, radiation or heat transfer coefficient. Another explanation for this is that the simulation does not take deformation in a forging process into consideration. The effect of deformation on precipitation kinetics was introduced in section 3.2.11 and with [27]. The deformation could be very high at forging at lower temperature regions and induce more σ than predicted in a theoretical simulation, without considering deformation. Now it is discussed that deformation can affect the kinetics for σ -precipitation and could be applied to the expansion stage. In the experiments, the expansion stage was generalized as a constant cooling rate in air, where deformation was dismissed. Even though deformation here is lower than in forging, it could imply that the results from expansion are missing an influencing parameter. It is possible that more σ could be present when deforming the material than what was conducted in the non-deformed experiments.

The relation between temperature and time would be of interest to further study in order to understand the underlying effects of deformation. Especially, since this mechanism could be related to the presence of σ -phase in expansion and extrusion.

6.3 QAsc3 result variation

Sample QAsc3 show different results between LOM and SEM compared to all other observations. Throughout the gathering of the results, there were similarities between LOM and SEM that darker irregular strokes seen in LOM would be confirmed to be σ in SEM/EDS. In LOM, for sample QAsc3, there were no signs of σ as it showed either no dotted lines or any continuous strokes, seen in Fig 41c. The only indication that precipitation was seen were very few faint dots at one line when looked at in 500x magnification. The observed boundary can be seen in the middle of the image in Fig 44. It is very faint, but at this magnitude, it is possible to see signs of small dots on the boundary. Compared to SEM, a magnitude of at least 2000x was required to clearly observe present precipitates in all samples. From a theoretical point of view, the time above $T_{\sigma MST}$ should not be enough to fully dissolve σ compared to Fig 18 (yellow label). It could indicate that the elemental composition is still there, i.e. σ has just been dissolved and in some cases, to a small extent, precipitates are left.

Although it is confusing that σ can be present even though it seems to be free in LOM, the scale at which σ is present in sample QAsc3 is at such a small degree that it would've been accepted in the final product.

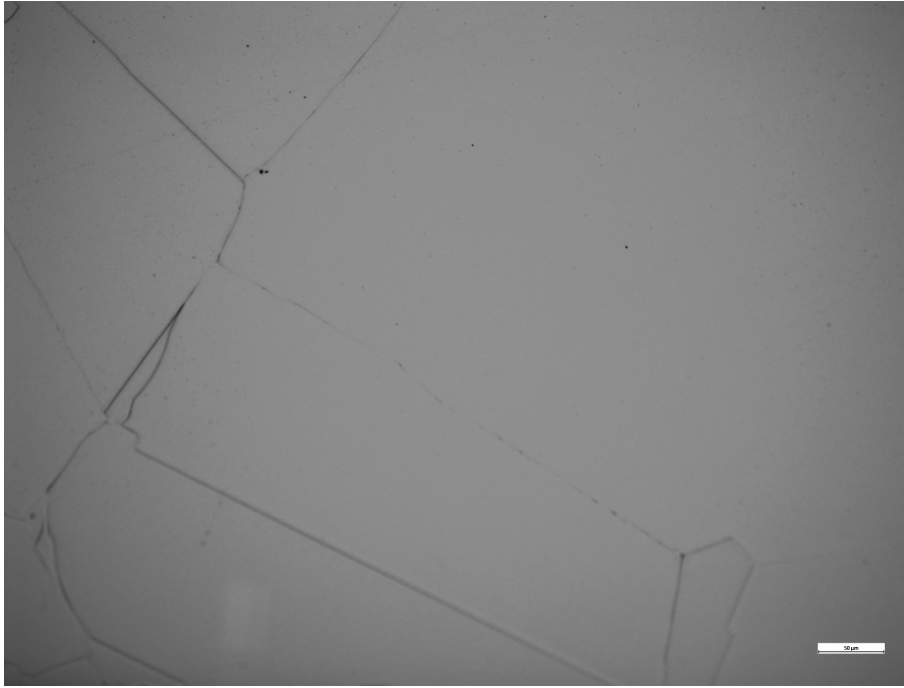


Figure 44: *Darkened image of sample QAsc3 at 500x magnification in LOM*

This discussion point can now lead to the difference between continuous or discontinuous lines observed between LOM and SEM. It is evident that some of the samples observed in LOM have continuous lines while they are discontinuous in SEM, an example can be observed when comparing Fig 36c and 40. The classification to what extent σ is present and if the product will be accepted or not is made in LOM. If continuous lines are seen in LOM the product is not accepted.

6.4 CWF implementation

The results obtained from the CWF simulations and results indicate that CWF is a plausible replacement for the quench-annealing stage. This is reasonable because a sigma-free structure was shown in this thesis to be obtainable from re-heating in a CWF right after forging. However, the method and results did not include a mapping of the elemental composition present in grain boundaries. Because the time in the furnace for the CWF is 20x shorter, it is possible that the elemental composition of recently dissolved σ is still left. A local region of an increment in Mo has been shown to increase $T_{\sigma MST}$ [12] and in Fig [10]. Combined with the results from Heating 1 and with an insufficiently heated region, it can increase the risk of σ precipitating at Mo-increased areas when processing during the expansion-extrusion stages.

To gather any idea of the composition left after CWF, theory can conclude this. In section 3.3.1, the values for time to dissolve and even out the elemental composition for σ were presented. All locations in their respective temperature to time obtains green and should not contain signs of σ composition. The only area which is at risk is at mid-surface, with close margins to being fully dissolved (yellow).

Although σ -free, the grain sizes in a CWF heat-treated bar differs from the sizes obtained from quench-annealing in a WBF. Grain sizes are ASTM 2.0 at the half radius and ASTM 1.0 at the outer surface samples. Compared to ASTM 0 for locations of quench-annealed samples. A slight decrease in grain size could affect the precipitation of σ by means of increasing the number of nucleation sites. Smaller grains mean an increased number of grain boundaries, as well as triple junctions. This is the only known risk, regarding σ -phase, of implementing a CWF presented in this thesis.

A change to a CWF instead of WBF requires work regarding logistics. The time of forging is half that of the time in CWF meaning that a batch of two bars would be most optimal to be able to fit into the CWF.

All things considered, the CWF shows to be a valuable choice of replacement to the quench-annealing stage for the manufacturing route. Considering σ -phase, chemical composition, grain sizes and energy savings.

6.5 Induction heating and soaking implementation

The results presented on Heating 1 showed that if temperatures don't reach above $T_{\sigma MST}$, it is most likely that σ either will precipitate or won't dissolve. Temperature regions that are of interest are the $T_{\sigma MST}$ regions. It is most probable that an outer top surface or inner surface could reach those temperatures if heating is insufficient. That could occur if, for example, a billet is released without holding time at Heating 1 top temperature, i.e. no cycling. The inner surface would've then not reached this temperature because of delayed heat transfer, explained in section 3.2.8. This region will have a lower temperature and that was shown in Heating 1 experiments to grow σ -phase.

If σ -phase grows during Heating 1 and expansion in a lower temperature region, the second induction furnace Heating 2 has the potential to be able to dissolve present σ . As mentioned in section 3.2.10 for Heating 2, the wall thickness is now thinner and the depth of penetration is now sufficient to heat the complete thickness of the billet. Additionally, it was shown from the stop scenario experiment in sample QAsc3 that a short period of time above $T_{\sigma MST}$ is enough to dissolve σ -phase with similar temperature-time curves, although with traces of chemical composition of σ -phase left. This would indicate that Heating 2 can justify insufficiently heated regions in Heating 1. Although, the time here is very short and should not entirely be relied on to secure a product free of σ after extrusion.

The latter leads to the potential of introducing soaking to secure a σ -free structure before extrusion. Both the dissolution areas presented in section 3.3.1 and the results from the soaking experiments showed that the time in soaking at those temperatures dissolves σ -phase. This would diminish the demands of having to sufficiently heat all regions above $T_{\sigma MST}$ in both induction furnaces. Instead, billets are only required to be heated in order to have high enough temperatures for expansion.

6.6 Full-scale experiments

All results given in this report were made through Gleeble thermal experiments. It gives high precision regarding time and temperature to perform real production and heat treatment procedures. However, many parameters in full scale can not be accounted for in this method. Gleeble thermal rods are homogeneous in temperature at the sampled volume, on the other hand, it might not resemble production exactly. If the margins are small, the results could show the difference between the samples at half-radius and outer radius. Another parameter undisclosed is the axial sample variation previously discussed. A third parameter not implemented in this report is the relation between temperature and deformation also previously discussed. So to say, it is important to note that this report and the experiments conducted showed indications of what the full-scale results could look like. The results presented clear directions for the simulated version of heat treatment. It is, although, of importance to continue this research with full-scale experiments to confirm the sightings as well as to be able to implement the ideas presented in this report.

7 Conclusions

- After forging, re-heating in a CWF is enough to dissolve σ -phase at half-radius and surface locations.
- Grain sizes obtained from a CWF differ between half-radius and surface by ASTM 2.0 to 1.0.
- According to Gleeble experiments, the CWF is a valuable replacement for the quench-annealing (WBF) stage.
- Temperatures below the heating 1 top temperature has a risk of inducing σ precipitation to varying degrees.
- If a region reaches Heating 1 top temperature in the first induction furnace, it is enough to dissolve σ -phase.
- Between the induction furnaces, i.e. expansion and transportation, no further σ -phase precipitation occurs. Based on Gleeble experiments without deformation.

7.1 Future Work

These are suggestions for further research into this problem, as well as what tasks are needed to implement the ideas presented in the discussion.

- Logistical approach on the implementation of a CWF after forging
- CWF full-scale experiment with sampling after CWF+quenching at varied longitudinal locations at 5 or more radial locations
- Investigation of the σ -precipitation relationship between temperature and degree of deformation
- Investigation into the relationship between grain size and rate of σ -precipitation at different temperatures

References

- [1] Agren J. The handbook for stainless steel in sandvik; 2005.
- [2] Askeland DR, Pradeed P F, Wendelin J W. The science and engineering of materials. 6th ed. Cengage; 2011.
- [3] Lebedev A, Kosarchuk V. Influence of phase transformations on the mechanical properties of austenitic stainless steels. International Journal of Plasticity. 2000;16(7-8):749-67.
- [4] Kain V. Stress corrosion cracking (SCC) in stainless steels. In: Stress corrosion cracking. Elsevier; 2011. p. 199-244.
- [5] Alleima. Sanicro®28 Tube and pipe, seamless. UNS: N08028;. Available from: <https://www.alleima.com/en/technical-center/material-datasheets/tube-and-pipe-seamless/sanicro-28/?show=pdf>.
- [6] Sourmail T. Simultaneous Precipitation Reactions in Creep-Resistant Austenitic Stainless Steels. Cambridge, UK: University of Cambridge;.
- [7] Turchi PE, Kaufman L, Liu ZK. Modeling of Ni–Cr–Mo based alloys: Part I—phase stability. Calphad. 2006;30(1):70-87.
- [8] Marshall P. Austenitic stainless steels: microstructure and mechanical properties. 1984.
- [9] Michler T. Austenitic Stainless Steels. In: Reference Module in Materials Science and Materials Engineering. Elsevier; 2016. Available from: <https://www.sciencedirect.com/science/article/pii/B9780128035818025091>.
- [10] Cortez OA, Moura FJ, de Albuquerque Brocchi E, de Siqueira RNC, de Souza RFM. Fe-Ni Alloy Synthesis Based on Nitrates Thermal Decomposition Followed by H₂ Reduction. Metallurgical and Materials Transactions B. 2014;45:2033-9.
- [11] Gich M, Shafranovsky E, Roig A, Ślawska-Waniewska A, Racka K, Casas L, et al. Aerosol nanoparticles in the Fe 1- x Cr x system: Room-temperature stabilization of the σ phase and $\sigma \rightarrow \alpha$ -phase transformation. 2005;98(2):024303.
- [12] Hsieh CC, Wu W. Overview of intermetallic sigma phase precipitation in stainless steels. International Scholarly Research Notices. 2012;2012.
- [13] Ardell A. The growth of gamma prime precipitates in aged Ni- Ti alloys. Metallurgical and Materials Transactions B. 1970;1:525-34.
- [14] Ramirez A, Lippold J, Brandi S. The relationship between chromium nitride and secondary austenite precipitation in duplex stainless steels. Metallurgical and materials transactions A. 2003;34(8):1575-97.
- [15] Raja V, Shoji T. Stress corrosion cracking: theory and practice. Elsevier; 2011.

- [16] Amuda MOH, Mridha S. An overview of sensitization dynamics in ferritic stainless steel welds. International Journal of Corrosion. 2011;2011.
- [17] ASTM. Methods for Determining Average Grain Size. ASTM International;. Available from: <https://www.astm.org/e0112-13r21.html>.
- [18] EVIDENT. Grain Size Analysis in Metals and Alloys;. Available from: <https://www.olympus-ims.com/en/applications/grain-size-analysis/>.
- [19] Kolmskog P. Pacman - Precipitation kinetics of sigma phase during extrusion of San28cu tubes. 2014-08-05;Technical Report 140893TE.
- [20] Nylöf L, Jakobsson K, Meurling F. Framtagande av ett upplösningsdiagram för sigmafas i Sanicro 28 stång. 2007-04-02;Technical Report 070405TE.
- [21] Vander Voort G. Metallography of superalloys. Industrial heating. 2003;70(10):40-3. Available from: <https://vacaero.com/information-resources/metallography-with-george-vander-voort/880-metallography-of-superalloys.html>.
- [22] Zhou W, Chen X, Wang Y, Chen K, Zhu Y, Qin J, et al. Microstructural Evolution of Wrought-Nickel-Based Superalloy GH4169. Metals. 2022;12(11):1936.
- [23] Hansson S, Fisk M. Simulations and measurements of combined induction heating and extrusion processes. Finite elements in analysis and design. 2010;46(10):905-15.
- [24] Haimbaugh RE. Practical induction heat treating. ASM international; 2015.
- [25] Meurling F. Sigmafas i vidgad och släckt extrusionskuts i San28Cu. 2007-10-02;Technical Report 070981TE.
- [26] Hansson S. Simulation of stainless steel tube extrusion. Luleå tekniska universitet; 2006.
- [27] Bignon M, Ma Z, Robson JD, Shanthraj P. Interactions between plastic deformation and precipitation in Aluminium alloys: A crystal plasticity model. Acta Materialia. 2023;247:118735.
- [28] Meurling F. Sigmafas i extrusionsfront hos San28Cu-hollows extruderade från släckglödgad stång. 2006-07-06;Technical Report 060807TE.
- [29] Meurling F. Dokumentering av mikrostruktur i kokillgjuten San28Cu stång av smidd, skalsvarvad dimension diam324mm, med resp. utan släckglödning i stegbalksugn 98 enligt strategi 100. 2007-05-22;Technical Report 070557TE.
- [30] Nylöf L. TTP-diagram for Sandvik Sanicro 28. 2009-11-03;Technical Report 091212TE.